Polymerization of Rod-Like Macromolecular Monomers Studied by Stopped-Flow, Multiangle Light Scattering: Set-Up, Data Processing, and Application to Fibrin Formation

Simonetta Bernocco,*‡ Fabio Ferri,§ Aldo Profumo,† Carla Cuniberti,‡ and Mattia Rocco*

*Gruppo di Biostrutture and †Servizio di Biologia Molecolare, Istituto Nazionale per la Ricerca sul Cancro, Centro per le Biotecnologie Avanzate, I-16132 Genova, ‡Dipartimento di Chimica e Chimica Industriale, Università di Genova, I-16146 Genova, and §Dipartimento di Scienze Chimiche, Fisiche e Matematiche, Università dell'Insubria a Como and INFM, I-22100 Como, Italy

ABSTRACT Many biological supramolecular structures are formed by polymerization of macromolecular monomers. Light scattering techniques can provide structural information from such systems, if suitable procedures are used to collect the data and then to extract the relevant parameters. We present an experimental set-up in which a commercial multiangle laser light scattering photometer is linked to a stopped-flow mixer, allowing, in principle, the time-resolved extrapolation of the weight-average molecular weight M_w and of the z-average square radius of gyration $\langle R_g^2 \rangle_z$ of the polymers from Zimm-like plots. However, if elongated structures are formed as the polymerization proceeds, curved plots rapidly arise, from which M_w and $\langle R_g^2 \rangle_z$ cannot be recovered by linear fitting. To verify the correctness of a polynomial fitting procedure, polydisperse collections of rod-like or worm-like particles of different lengths, generated at various stages during bifunctional polycondensations of rod-like macromolecular monomers, were considered. Then, the angular dependence of their time-averaged scattered intensity was calculated in the Rayleigh–Gans–Debye approximation, with random and systematic noise also added to the data. For relatively narrow size distributions, a third-degree polynomial fitting gave satisfactory results across a broad range of conversion degrees, yielding M_w and $\langle R_g^2 \rangle_z$ values within 2% and no greater than 10–20%, respectively, of the calculated values. When more broad size distributions were analyzed, the procedure still performed well for semiflexible polymers, but started to seriously underestimate both M_w and $\langle R_g^2 \rangle_z$ when rigid rod-like particles were analyzed, even at relatively low conversion degrees. The data were also analyzed in the framework of the Casassa approximation, from which the mass per unit length of the polymers can be derived. These procedures were applied to a set of data taken on the early stages of the thrombin-catalyzed polymerization of fibrinogen, a rod-like macromolecule ~50 nm long. The polymers, grown in the absence of Ca^{2+} by rate-limiting amounts of thrombin, appeared to be characterized by a much broader size distribution than the one expected for a classical Flory bifunctional polycondensation, and they seem to behave as relatively flexible worm-like double-stranded chains. Evidence for the formation of fibrinogen–fibrin monomer complexes is also inferred from the time dependence of the mass/length ratio. However, our data are also compatible with the presence of limited amounts of single-stranded structures in the very early stages, either as a secondary, less populated pathway, or as transient intermediates to the classical double-stranded fibrils.

INTRODUCTION

Light scattering techniques can provide a number of size- and shape-related solution parameters traditionally used for the characterization of macromolecules or particles (reviewed in Huglin, 1972; Schmitz, 1990; Harding et al., 1992). In the "static" mode, it is possible to recover, from the angular dependence of the time-averaged intensity of the scattered light, the weight-average molecular weight M_w and the z-average square radius of gyration $\langle R_g^2 \rangle_z$ of polydisperse macromolecular systems. This is usually done by recording with a moving detector the intensity of the scattered light at a number of angles in the plane of the incident beam, and then applying extrapolation procedures to zero scattering angle. Although this procedure is normally used to characterize macromolecular solutions in thermodynamic equilibrium conditions, it is also possible to follow the time evolution of M_w and $\langle R_g^2 \rangle_z$ for solutions away from equilibrium, such as during a polymerization reaction. However, in the traditional set-up described above, this is possible only for very slow reactions, because the detector can collect the scattered light only at one angle at a time, and several angles are needed, each with a finite collection time, to obtain statistically meaningful results. This bottleneck can be, now at least, partially bypassed by the advent of light scattering photometers of a different design, in which the scattered light is collected at many angles simultaneously by a number of fixed detectors. One commercially available instrument, the DAWN-DSP from Wyatt Technology Corp. (Santa Barbara, CA), was developed as an on-line detector for gel-permeation/size-exclusion chromatography, and is equipped with a solid glass cylindrical cell, with a flow-through small horizontal bore, around which eighteen photodiodes are positioned at fixed angles (see Fig. 1). The combination of a flow-through cell and multiangle laser light scattering (MALLS) detection renders this instrument very well suited for recovering the physicochemical parameters of macromolecular solutes away from equilibrium

Received for publication 25 May 1999 and in final form 21 March 2000.

Address reprint requests to Dr. Mattia Rocco, Gruppo di Biostrutture, Centro Biotecnologie Avanzate (CBA), Largo Rosanna Benzi 10, I-16132 Genova, Italy. Tel.: +39-0105737-310; Fax: +39-0105737-325; E-mail: rocco@ermes.cba.unige.it.

0006-3495/00/07/561/23 $2.00

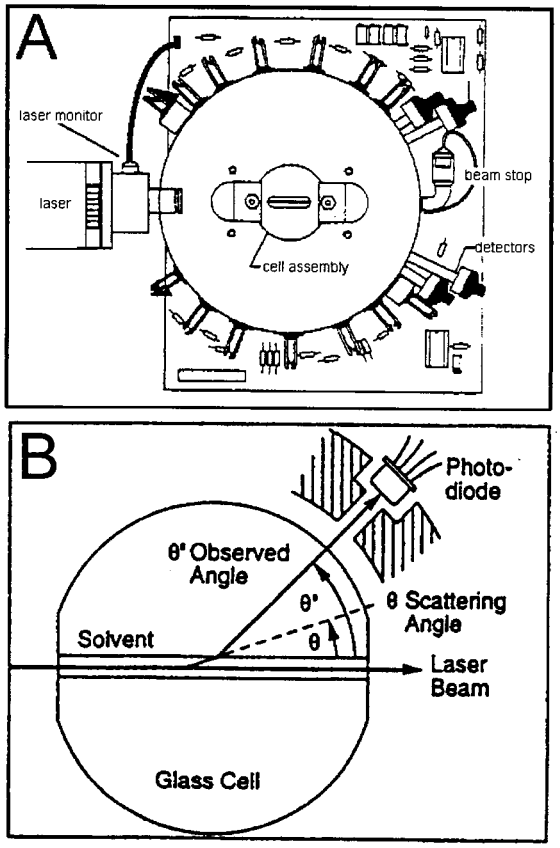

FIGURE 1 Schematic drawing of the DAWN-DSP-F photometer. (*A*) Head of the instrument with the eighteen fixed detectors. (*B*) Glass flow-through cell with one photodiode shown (both panels reproduced with permission of Wyatt Technology Corp.).

conditions, such as during polymerization and aggregation processes, nucleation and growth of crystals, etc.; when coupled with a rapid mixing device, these reactions can be followed with a time resolution of at least a few tenths of a second.

In this paper, we describe the experimental set-up for the stopped-flow/MALLS system used by us. Furthermore, because we are currently interested in the polymerization of rod-like macromolecular monomers, we have performed a series of numerical tests to ascertain if the data analysis routines available with the instrument software could recover from Zimm-like plots (Zimm, 1948) the standard parameters, M_w and $\langle R_g^2 \rangle_z$, of synthetic data within a reasonable range of error. In addition, the experimental data were also reduced in the framework of the Casassa approximation (Casassa, 1955), from which the mass/unit length M_L of ensembles of long rods, polydisperse both in thickness and length, could be derived. To show the potential afforded by the simultaneous determination of M_w and $\langle R_g^2 \rangle_z$, together with M_L, of evolving polymers, we report a set of data on a very important physiological reaction: the supramolecular polymerization of fibrinogen.

Fibrinogen (FG) is a high molecular weight (340,000), rod-like (~46–50 nm long) glycoprotein made up by three pairs of different polypeptide chains (2Aα, 2Bβ, and 2γ) joined together by disulfide bonds to give a symmetric particle (see Mosesson and Doolittle, 1983; Doolittle, 1984). The N-terminal ends of all the chains are contained within a central E domain, from which they depart to form two triple coiled-coils connectors ending in two outer D domains, each containing the C-terminal ends of the Bβ and γ chains. The C-terminal ends of the Aα chains (>400 amino acids) do not enter the D domains and seem to fold back to form a fourth domain positioned above the central one (Mosesson et al., 1981; Erickson and Fowler, 1983; Medved' et al., 1983; Weisel et al., 1985; Spraggon et al., 1997). FG is activated by thrombin, which sequentially removes first a pair of small peptides called fibrinopeptides A (FPA), and later on a second pair (fibrinopeptides B, FPB) from the N-terminal ends of the Aα and Bβ chains, respectively. The resulting fibrin monomers [$(\alpha\beta\gamma)_2$] polymerize forming rod-like fibrils, which, by branching and lateral aggregation, give rise to a three-dimensional network (see Mosesson and Doolittle, 1983; Doolittle, 1984; Mosesson, 1990; Blombäck, 1996). Two sets of complementary knob–hole interactions between sites uncovered by the removal of the fibrinopeptides in the central E domain (the knobs or A and B sites) with sites always available in the outer D domains (the holes or *a* and *b* complementary sites) have been convincingly demonstrated to play a major role in fibrin formation. Under physiological conditions, the A–*a* interactions are responsible for the linear elongation of the polymers into half-staggered, double-stranded "protofibrils", whereas the B–*b* interactions influence their subsequent lateral aggregation, (Laurent and Blombäck, 1958; Fowler et al., 1981; Weisel, 1986; Medved' et al., 1990; Weisel et al., 1993; Spraggon et al., 1997; Everse et al., 1998; and references therein). However, the specificity of these processes is highly dependent on the nature and concentration of the ions present in solution (see Di Stasio et al., 1998, and references therein). Whereas the general mechanism of fibrin formation is now quite well understood, several issues are still controversial. In particular, the early stages leading to the formation of the protofibrils, and the onset of branching, a fundamental requisite for the formation of a three-dimensional network, remain to be elucidated.

Light scattering techniques have been applied in the past to the study of fibrin polymerization, but the constraint of measuring the scattered intensity at one single angle at a time was a major limitation. Different ways have been followed to overcome this problem, with a series of important papers appearing ~20 years ago (references to earlier work can be found in Sheraga and Laskowski, 1957; studies using mainly dynamic light scattering, like the recent one by Bauer et al., 1994, will not be dealt with here). In particular, the kinetic aspect of fibrin polymerization was studied by

measuring the intensity of scattered light at right angle only (Hantgan and Hermans, 1979), or by determining M_w as a function of reaction time at relatively high ionic strength (0.5 M NaCl) after collecting, almost simultaneously, the light scattered at nine different angles (Visser and Payens, 1982). Alternatively, more structural data were collected after the process had been slowed down by using very low thrombin amounts (Müller and Burchard, 1978; Müller et al., 1981; Wiltzius et al., 1982a,b; Bauer et al., 1994) or by the addition of an inhibitor of fibrin polymerization (Knoll et al., 1984). All these studies have added important elements to the general picture, but because of the lack of *both* time- and *true* angle-resolved collection, they could not provide the necessary details for a better understanding of the earliest stages of the fibrinogen–fibrin conversion. In particular, the works of Müller and Burchard (1978) and of Wiltzius et al. (1982a) have suggested the presence of end-to-end polymers following enzyme activation, apparently at odds with the accepted mechanism for the initial events, the formation of half-staggered, double-stranded polymers. However, the most convincing evidence for this mechanism, apart from the biochemical data, has been mainly provided by electron microscopy (EM) (Fowler et al., 1981; Janmey et al., 1983b; Medved' et al., 1990; Weisel et al., 1993), which unfortunately suffers from poor time resolution and requires sample manipulation. Thus, providing accurate, time-resolved structural data from unperturbed solutions could help to clarify this issue.

The simultaneous determination with our stopped-flow/MALLS system of M_w, $\langle R_g^2 \rangle_z$, and M_L for the growing fibrin polymers after activation by thrombin in near physiological conditions, but in the absence of added Ca^{2+} and in the presence of EDTA-Na_2, has confirmed many previous observations and has yielded some preliminary new intriguing results. Theoretical curves calculated for various polymerization mechanisms of bifunctional rod-like monomers are also presented to tentatively interpret the data.

MATERIALS AND METHODS

Protein purification and quality control

All chemicals were reagent grade from Merck (Darmstad, Germany), unless otherwise stated, and double-distilled water was used in the preparation of all the solutions. Lyophilized human fibrinogen (TF grade, IMCO, Stockholm, Sweden) was dissolved at 37°C at a nominal concentration of 20 mg ml^{-1} in 0.3 M NaCl, to which were added 10 units/ml KIR (serine proteases inhibitor, Richter, Milano, Italy). It was then dialyzed at 4°C for 18 h against two changes of TBS buffer (50 mM Tris, 104 mM NaCl, 1 mM EDTA-Na_2, KIR 10 u/ml, pH 7.4). The dialyzed solution was centrifuged at 30,000 × *g* for 30 min, divided into aliquots, and stored at −80°C. FG concentrations were determined from the absorbance at 280 nm using a specific absorption coefficient E of 1.51 ml mg^{-1} cm^{-1} (Mihalyi, 1968), after correcting for scattering contributions by subtracting the absorbance at 320 nm. A Beckman DU640 spectrophotometer (Beckman Analytical, Milano, Italy) was used for absorption measurements. Thrombin from human plasma (T-6884, lyophilized from Na citrate) was from Sigma-Aldrich (Milano, Italy). It had a nominal activity of ~2000 NIH units/mg protein, was reconstituted with water to a final nominal concentration of 1000 NIH units/ml, and was stored in small aliquots at −80°C.

Before stopped-flow experiments, fibrinogen was further purified from its aggregates by gel filtration chromatography by loading 2–3 ml of stock solution on a glass column (1.5 × 167 cm) filled with Sepharose CL-4B (Pharmacia Biotech, Uppsala, Sweden), eluted at 6 ml h^{-1} at room temperature. The pooled peak fractions were furthermore centrifuged at 38,000 × *g* for 1 h (20°C). The purity of FG was tested by polyacrylamide (PAA) gel electrophoresis in the presence of sodium dodecyl sulfate (SDS-PAGE) of samples either nonreduced or reduced with dithiothreitol (Sigma) according to Laemmli (1970), using electrophoresis-grade reagents from Bio-Rad (Hercules, CA). The results of the purification steps are shown in Fig. 2, where a typical chromatogram is reported, together with the SDS-PAGE analysis on a 5% PAA gel of unreduced samples of the starting material, of two peak fractions and of the final pooled material, all at the same nominal protein loading concentration (*inset A*, *lanes 1–4*, respectively). As can be seen in Fig. 2, the high molecular weight species present, albeit in low amounts, in the starting FG sample (*inset A*, *lane 1*), gave rise to detectable humps in the chromatogram. The asymmetric main chromatographic peak resulted also from the incomplete separation of the doublet corresponding to various monomeric FG species differing by the extent of C-terminal degradation of the α-chains (see below), as evidenced by the electrophoretic analysis of two representative fractions (*arrows*; *inset A*, *lanes 2* and *3*). By taking only the main peak fractions (*shaded area*), nearly all the aggregates were removed (*inset A*, *lane 4*), leaving the FG doublet (more clearly seen when roughly one-fourth of sample was loaded on the gel as shown in inset *A*, lane 5). Rather than attempting a difficult and material-consuming separation between these two closely related species, we have performed a careful analysis of their composition. This was done by blotting on nitrocellulose sheets (Towbin et al., 1979) gels loaded and run with reduced peak FG samples, followed by immunostaining with the Y18 monoclonal antibody (a gift of Dr. W. Niuwenhuizen, Leiden, The Netherlands), which recognizes an epitope on the FPA (Koppert et al., 1985). Color was developed using a horseradish peroxidase-conjugated goat anti-mouse IgM secondary antibody (Southern Biotechnology Associates, Birmingham, AL) and 4-chloro-1-naphtol (Fluka

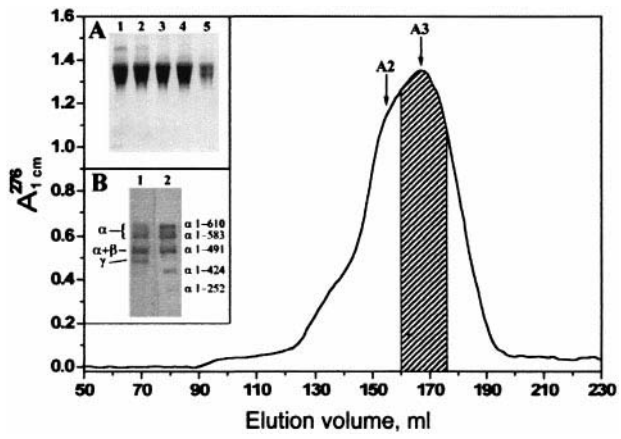

FIGURE 2 Elution profile of a fibrinogen solution (c = 16.4 mg ml^{-1}; 2 ml loaded) from a 1.5 × 167-cm Sepharose CL-4B chromatography column, monitored at λ = 276 nm. (*A*) The nonreduced SDS-PAGE analysis on 5% PAA gel of the starting material (*lane 1*), of two fractions (*lanes 2–3*) collected at the points indicated as A2 and A3 (*arrows*) in the main figure, and of the pooled material (*shaded area*) (*lanes 4–5*). Loaded amounts: lanes 1–4, 9 μg; lane 5, 2.5 μg. (*B*) A Western blot of the reduced pooled material after SDS-PAGE separation on a 8% PAA gel is shown stained with amido black (*lane 1*) or immunostained after reaction with the Y18 monoclonal antibody (*lane 2*).

Chemie, Buchs, Switzerland) as a substrate. In inset *B* of Fig. 2, a blot of a reduced pooled peak FG sample run on an 8% PAA gel and stained with amido black (*lane 1*) and its immunostained counterpart (*lane 2*) are shown. The immunostained blots were then scanned on a Mustek MFS 6000CX flatbed scanner using a 300 × 300 dots-per-inch resolution, and the area of each band was quantified with the One-Dscan software (Scanalytics, CSPI, Billerica, MA) with Gaussian deconvolution of overlapping peaks. The molecular weight of each αA chain species (identified on the left side of lane 2 in inset *B*) was deduced from the relative migration of each band, and checked against the calculated molecular weights of FG fragments derived from the potential plasmin cleavage sites in the αA-chains C-terminal portion, as will be reported in more detail elsewhere (Lai M. E., G. Franzoni, A. Profumo, C. Cuniberti, and M. Rocco, in preparation).

Multiangle laser light scattering (MALLS)

Static light scattering experiments were carried out with the multiangle photometer DAWN-DSP-F (Wyatt Technology Corp., Santa Barbara, CA) equipped with a 5-mW He-Ne laser source ($\lambda = 632.8$ nm), a K5 glass flow cell, and Peltier control of the temperature, which was kept at 25.0 ± 0.2°C. The true scattering angles seen by the fixed detectors in the DAWN-DSP-F depend on the refractive index of both the cell ($n = 1.52064$) and the solvent used (Wyatt Technology, 1997), and, under our conditions, 17 angles ranging from 4.7° to 158.1° were theoretically available. However, the two lower angles, positioned at 4.7° and 14.8°, are very noisy when aqueous solvents are used, and the practical range of the instrument was thus limited to fifteen angles from 21.9° to 158.1°.

The index of refraction of the buffer was measured at 589.3 nm and at 25°C by an Abbé refractometer and then interpolated at 632.8 nm at 25°C by using the same λ^{-2} dependence calculated for water from literature data (Lange, 1967). A value of 1.334 was found for TBS. For the fibrinogen solutions, a refractive index increment (dn/dc) of 0.192 ml mg^{-1}, (Carr et al., 1977) obtained by interpolation from literature data (Schulz and Ende, 1963), was used.

Spectroscopic grade toluene (Uvasol, Merck) directly filtered in the flow-through scattering cell through 25 mm diameter, 0.22 μm pore-size PTFE syringe filters (Acrodisc CR, Gelman Sciences, Ann Arbor, MI), was used for the absolute calibration of the MALLS photometer. A refractive index of 1.4912 (Timmermans, 1965) and a Rayleigh ratio of 1.414×10^{-5} cm^{-1} (Forziati, 1950; Forziati et al., 1950) at 632.8 nm and 25°C were used, respectively. Normalization of the fifteen photodiodes, to correct for their different responses, posed a very difficult problem. According to manufacturer instructions, when the flow-cell is used with aqueous solvents in the micro-batch mode, normalization of the detectors should be done by injecting a solution of a monodisperse low molecular weight polymer, filtered through 0.02-μm pore-size syntherized syringe filters (ANOTOP 25, Whatman, Maidstone, UK), and then assuming isotropic distribution of the scattered light. We tested both dextran ($M_w = 40{,}000$, a gift of Dr. D. Friscione of Alfatech, Genova, Italy) at a concentration of 3.3 mg ml^{-1}, and poly(ethylene glycol) ($M_w = 2700$–3300, cat. 81230, Fluka Chemie), at a concentration of 18 mg ml^{-1}, both filtered as stated above after centrifugation for 30 min at 38,000 × *g*, but this procedure was found to be unsatisfactory, especially at the lower angles. Alternatively, the detectors of the MALLS photometer can be normalized in the chromatography mode, by injecting into a size-exclusion (SE) chromatography system a solution of a globular protein of small R_g, and using only the monomer's peak slices from the chromatogram (Wyatt Technology, 1997). Bovine serum albumin (BSA, A-0281, Sigma; $R_g = \sim 2$ nm) was dissolved in TBS at 5 mg ml^{-1}, filtered through cellulose acetate 0.2 μm pore-size microcentrifuge filters (SPIN-X, Corning Costar, obtained through Sigma-Aldrich) and 200 μl were injected on a size-exclusion high pressure liquid chromatography (HPLC) set-up consisting of a 6 × 40 mm TSK-GEL PW_{XL} guard column (TosoHaas, Stuttgart, Germany) and three 7.8 × 300 mm TSK-GEL analytical columns ($G5000PW_{XL}$, $G4000PW_{XL}$, $G3000PW_{XL}$, TosoHaas) connected in series and operated at 0.3 ml min^{-1} from a System Gold HPLC system (Beckman) composed of 126 Solvent Module and 166 UV/VIS Concentration Detector. To further remove dust and particulate as much as possible, two on-line stainless steel filters (pore size 0.5 μm and 0.2 μm) were placed in series before the guard column, and another 0.2 μm pore size on-line stainless steel filter was placed right after the columns. The concentration of the eluted BSA was measured at 280 nm by the UV/VIS concentration detector module placed before the MALLS detector, using an extinction coefficient *E* of 0.66 ml mg^{-1} cm^{-1} (Edwards et al., 1969).

Stopped-flow MALLS: experimental set-up

The experimental stopped-flow MALLS apparatus used to follow the time evolution of fibrin polymerization is schematically represented in Fig. 3. It is composed of three parts: the injection device (a RX-1000 rapid mixing device from Applied Photophysics, Leatherhead, UK), the MALLS photometer, and a 100-μl, 10-mm pathlength square Suprasil quartz flow-through cuvette (Hellma, Müllheim, Germany) directly connected to the exit of the light scattering cell. The cuvette can be disconnected and placed inside a spectrophotometer for absorbance measurements.

The injection device consisted of two glass Accudil syringes (Hamilton, Bonaduz, Switzerland) simultaneously driven by a metal plate, which can be operated either manually or via a pneumatic drive. Each of the two 2.5-ml syringes is screwed on a Teflon block containing a three-way T-valve, with an inlet luer port and an outlet Teflon line exiting from it. The two syringes were filled via the inlet ports through additional three-way nylon luer-lock T-valves (Sigma), to which 25-mm-diameter, 0.22-μm-pore-size Millex-GP filters were attached, permitting the refill operations to be carried out with all-polypropylene syringes without introducing any dust or contaminants. Priming/normalizing operations can also be carried out through these three-way valves, without affecting the outlet lines. These lead to a machined Teflon "reverse Y" mixer (the two inlet lines enter in a V conformation, and the outlet line exits from the apex of the V from the same side as the inlet lines; a small mixing chamber is

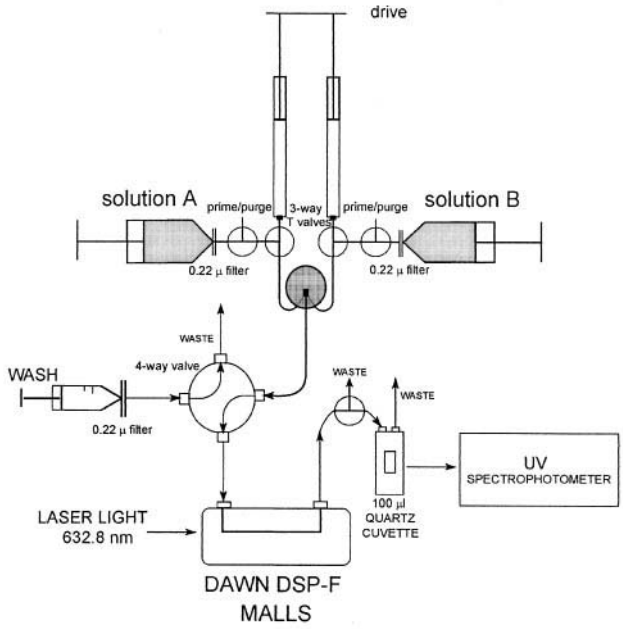

FIGURE 3 Experimental set-up for the stopped-flow/MALLS experiments (see Materials and Methods for details).

machined by slightly prolonging the outlet bore from the V apex). From the mixer, the outlet leads to a solvent-resistant four-way valve (SV-4, Pharmacia Biotech), from which the flow can be switched either to a waste line or to the flow cell of the MALLS photometer. The remaining port of the four-way valve is directly connected by a small PTFE tubing with a female luer lock fitting to a 20-ml polypropylene syringe to which a 25-mm-diameter, 0.22-μm Millex-GP filter is attached. At the exit of the MALLS cell, an inert three-way T-valve (HV3-3, Hamilton) allows the solutions to pass either through the UV cuvette or go directly to waste. Before the mixer, another three-way inert T-valve is inserted on one of the two mixing lines (not shown in Fig. 3), to allow the priming of the lines and of the mixing chamber when the glass syringes' content is changed, and their washing after the reaction is started. Immediately after every injection, the three-way valve after the MALLS cell is switched to an all-closed position, to avoid disturbing the solution in the cell by drainage/outgassing effects.

At the beginning of an experiment, the whole system was filled and washed with TBS buffer several times until reasonably dust-free, and then an injection was made and the baselines of the MALLS detectors recorded, with a data point every 0.25 seconds, in a new file on a Pentium PC computer directly connected to the A/D board of the DAWN-DSP-F, using the software ASTRA 4.60.07 (Wyatt Technology). The baseline UV spectrum was also recorded from the 100-μl cuvette. Then syringe A was filled (with normalization/priming) with a fibrinogen solution at twice the desired final concentration, syringe B was refilled with buffer, and a second injection was made, allowing the recording on the same file of the intensity of the light scattered by fibrinogen, as well as measurement of its real concentration in the mixture from the UV cuvette reading. Subsequently, syringe A was refilled with fibrinogen, syringe B was filled (with normalization/priming up to the valve before the mixer) with a thrombin solution (at nominal 0.25 NIH units/mg FG, final concentration), and the experiment was started by the injection of the reaction mixture in the flow cell. The measuring cell was then locked by turning the 4-way valve in the direction of the washing syringe, and the mixer and the outlet lines were immediately washed with TBS by connecting another polypropylene syringe with a 0.22-μm filter to the three-way valve attached just in front of the mixer (not shown on Fig. 3). The mixing operation and solution transfer were made by hand-driving the metal plate, and took less than 3 s. The complete intensity data were collected in the same file where blank and fibrinogen data were recorded. Because we were interested in the early stages of fibrin polymerization, the reaction was usually stopped before the intensity of the scattered light saturated the detectors, well before a recognizable clot was formed in the cell. Therefore, up to three reactions could be recorded on a single file, and, between them, the flow-through scattering cell was carefully washed via the external syringe until back to starting conditions.

Light scattering theory

For infinitely dilute macromolecular solutions, the excess intensity of scattered light recorded as a function of the angle θ between the primary and the scattered beam, expressed as the Rayleigh ratio R_θ (cm^{-1}), is given by the sum of the contributions from the single particles,

$$R_\theta = Kc \sum_{i=1}^{N} w_i M_i P_i(\theta), \tag{1}$$

where c is the sample concentration (g cm^{-3}), and K is the optical constant (cm^2 mol g^{-2}), equal to $4\pi^2 n^2 (dn/dc)^2/(N_A \lambda^4)$, n being the refractive index of the solvent, dn/dc the refractive index increment of the solute in that particular solvent, λ the wavelength in vacuo and N_A the Avogadro number. M_i is the molecular weight of the ith particle, w_i its corresponding weight fraction, and the adimensional function $P_i(\theta)$ represents the particle scattering factor, which is normalized to unity for $\theta = 0$, i.e., $P(\theta = 0) = 1$. Expressions of $P(\theta)$ for particles of various geometries are available in the Rayleigh–Gans–Debye (RGD) approximation (see Huglin, 1972), and, in this paper, we will be dealing with either rigid rod-like particles or semiflexible worm-like chains. For a rod-like particle of length L, the form factor is given by

$$P(x) = \frac{2}{x}\int_0^x \frac{\sin z}{z}\,dz - \left[\frac{\sin(x/2)}{x/2}\right]^2, \tag{2}$$

with $x = qL$, q being the scattering wavevector given by $q = (4\pi n/\lambda)\sin(\theta/2)$. For semiflexible worm-like chains, we can refer to the expression developed by Koyama (1973),

$$P(q) = \frac{2}{L_c^2}\int_0^{L_c} (L_c - t)\varphi(t, l_k, q)\,dt, \tag{3}$$

where L_c is the contour length of the chain, l_k is the Kuhn statistical segment length (equal to two times the persistence length l_p), and the function φ is defined elsewhere (Koyama, 1973). It is worth noticing that, when the ratio $\beta = l_p/L_c \gg 1$, the chain is infinitely stiff and behaves as a rigid rod, with Eq. 3 reducing to Eq. 2.

In any case, even when the expression of $P(\theta)$ is not known, the RDG theory predicts that the behavior of the scattered intensity distribution becomes independent of particle shape as θ approaches 0. Under this limiting condition, it is convenient to follow the data treatment first suggested by Zimm (1948):

$$\frac{Kc}{R_\theta} = \frac{1}{M_w}\left(1 + \frac{16\pi^2 n^2 \langle R_g^2\rangle_z}{3\lambda^2}\sin^2\frac{\theta}{2}\right). \tag{4}$$

Thus, the weight-average molecular weight,

$$M_w = \sum_i w_i M_i, \tag{5}$$

and the mean square z-average radius of gyration,

$$\langle R_g^2\rangle_z = \sum_i w_i M_i R_g^2(i) \Big/ \sum_i w_i M_i, \tag{6}$$

can be obtained from the intercept, and from the ratio between the slope and the intercept, respectively, of the plot of Kc/R_θ versus $\sin^2(\theta/2)$. Strictly speaking, measurements at various concentrations should be performed and the data extrapolated to zero concentration, but, because of the low fibrinogen concentration used by us (between 0.1 and 0.35 mg/ml), this dependence is neglected here. Equation 4 is applicable only to a limited range of dimensions or angles, i.e., when the second term inside the right-hand side parentheses is $\ll 1$. When this term approaches unity, the Zimm plot deviates from a linear behavior (for example, a value of 0.2 gives deviations of about a few percents), and its curvature depends on the particular structure of the particles being studied. Thus, no direct information on the parameters M_w and $\langle R_g^2\rangle_z$ can be easily recovered in this case, unless smaller scattering angles become available.

In the case of polydisperse solutions of rod-like (or worm-like) particles, a second treatment derived by Casassa (1955) can be used. The Casassa method is applicable in a range of angles and particle sizes that is opposite from that of the Zimm plot: for rod-like particles ($l_p/L_c \gg 1$), the condition is $qL_c > 3.8$ (and not >1.5 as stated in Wiltzius et al., 1982b), whereas, for semiflexible worm-like chains, two conditions must be satisfied, $qL_c > 3.8$ and $ql_p > 1.9$ (see also Koyama, 1973; Yamakawa and Fujii, 1974). When the above requirements are met, $(R_\theta)^{-1}$ is linearly

related to $\sin(\theta/2)$ and, from the slope of the plot of Kc/R_θ versus $\sin(\theta/2)$,

$$\frac{Kc}{R_\theta} = \frac{2}{\pi^2}\frac{\sum_i \frac{M_i w_i}{L_c^2(i)}}{\left(\sum_i \frac{M_i w_i}{L_c(i)}\right)^2} + \frac{4n}{\lambda \sum_i \frac{M_i w_i}{L_c(i)}}\sin\frac{\theta}{2}, \qquad (7)$$

one can recover the average mass for unit length $M_L = \Sigma_i M_i w_i / L_c(i)$, where $L_c(i)$ represent the contour length of the ith chain.

Data analysis and simulations

The collected MALLS intensity profiles were analyzed first using the software provided by the instrument's manufacturer, ASTRA version 4.60.07 (Wyatt Technology). Briefly, the baselines were set, including a "fake" baseline for the UV detector signal, generated to reproduce the actual fibrinogen concentration as measured from the UV cuvette, and "peaks" regions were selected (the software was originally developed for analyzing chromatography data, and, although a microbatch option is provided, none is unfortunately available for the treatment of kinetic data). The selected regions were then analyzed via the Debye plot option of the software, which is a Zimm-like plot without the concentration dependence of the data. The Kc/R_θ versus $\sin^2(\theta/2)$ data for each time slice were then fitted with either a first-degree or a third-degree polynomial, to recover M_w and $(\langle R_g^2\rangle_z)^{1/2}$ from the intercept and from the ratio between the initial slope and the intercept, respectively, of the fits. Each complete set of time slices containing the M_w and $(\langle R_g^2\rangle_z)^{1/2}$ data, together with their calculated standard deviations, can be downloaded to an ASCII file by the software.

For the analysis of the data by the Casassa equation, the Rayleigh ratios R_θ calculated at the various angles had to be downloaded from the software as an ASCII file, and were processed using the ORIGIN 4.0 software (Microcal Software Inc., Northampton, MA). Unfortunately, because the ASTRA software does not download the standard deviations associated with the R_θ, these had to be computed again from the baseline values, and may slightly differ from those calculated by ASTRA (see United States Patent 5,528,366, 1996).

To ascertain the validity of the data analysis based on the polynomial fittings of the Zimm plots, we carried out several numerical simulations trying to match as much as possible the experimental conditions. First, we assumed to have a polydisperse dilute solution of either rod-like or worm-like particles characterized by a mass distribution typical of bifunctional polycondensation models in which the monomers are rods of length L_0 = 50 nm and diameter $d_0 \sim 3$ nm, for a volume of 357 nm^3 corresponding to that calculated from the amino acid sequence of anhydrous FG. The 50-nm FG length was chosen over the 46–48-nm length deduced from EM data (Hall and Slayter, 1959; Mosesson et al., 1981; Erickson and Fowler, 1983; Weisel et al., 1985), because, from our SE-HPLC-MALLS solution data, an R_g of 14.5–15 nm was consistently found for monomeric FG (Bernocco, 1998; see Results). A density of 1.395 g ml^{-1} was assumed, so that the molecular weight of the monomers is $M_0 = 3.0 \times 10^5$ g mol^{-1} (see Results for the reason for this assumption). The most-probable size distribution predicted by the bifunctional polycondensation model with sites all having equal reaction probability, expressed in terms of the weight fraction $w_i(p)$ of the ith polymer made of i monomers, is the Flory distribution (Flory, 1936, 1942, 1953):

$$w_i(p) = i(1-p)^2 p^{(i-1)}, \qquad (8)$$

where the parameter p represent the conversion degree of the monomers, related to the number-average polymerization degree α by the relation $\alpha = 1/(1-p)$.

Size distributions were also calculated in the framework of the theory developed by Janmey (Janmey, 1982; Bale et al., 1982). In this case, it was supposed that the rate of removal of the two FPA from each FG molecule is not equal, but that the second is released faster than the first by a factor Q. This leads to a distribution of unreactive $(A\alpha B\beta\gamma)_2$, monofunctional $A(\alpha B\beta\gamma)_2$, and bifunctional $(\alpha B\beta\gamma)_2$ species whose time-dependent concentrations (referred to hereafter as $[A_2\alpha_2]_t$, $[A\alpha_2]_t$, and $[\alpha_2]_t$, respectively) can be calculated, given the initial fibrinogen $[F_0]$ and thrombin [Th] concentrations, from the following set of two differential and one linear equations (Janmey, 1982):

$$-\frac{d[A_2\alpha_2]_t}{dt} = \frac{2K_2[Th][A_2\alpha_2]_t}{K'_M + (2[A_2\alpha_2]_t + [A\alpha_2]_t)}, \qquad (9)$$

$$\frac{d[\alpha_2]_t}{dt} = \frac{QK_2[Th][A\alpha_2]_t}{K'_M + (2[A_2\alpha_2]_t + [A\alpha_2]_t)}, \qquad (10)$$

$$[A_2\alpha_2]_t = [F_0] - [A\alpha_2]_t - [\alpha_2]_t, \qquad (11)$$

where K_2 (7.3×10^{-7} M[(NIH units ml^{-1})s]$^{-1}$) is the rate constant for the liberation of one bovine FPA by bovine thrombin and K'_M is a Michaelis–Menten constant, which takes into account the competition between bovine Aα and Bβ chains for bovine thrombin (Martinelli and Scheraga, 1980; Janmey, 1982; Bale et al., 1982),

$$K'_M = K_M\left(1 + \frac{[B\beta]}{K_{MB}}\right), \qquad (12)$$

where $K_M = 9.2 \times 10^{-6}$ M, $K_{MB} = 11.3 \times 10^{-6}$ M (Martinelli and Scheraga, 1980), and [Bβ] is the concentration of intact Bβ chains. For the early stages of the reaction, it can be safely assumed that $[B\beta] = 2[F_0]$. To match our experimental conditions, we set $[F_0] = 1.2 \times 10^{-6}$ M, resulting in $K'_M = 1.12 \times 10^{-5}$ M, and values of [Th] between 0.05 and 0.17 NIH units ml^{-1} were chosen. After substitution of Eq. 11 in Eqs. 9 and 10, numerical integration with a Runge–Kutta method using LabVIEW 5.1 (National Instruments, Austin, TX) yielded the concentration of the reacting species as a function of discrete time steps.

The time-dependent size distribution of polymers formed by the random association of a mixture of monofunctional and bifunctional units was derived by Janmey (1982) apparently starting from the work of Flory on linear polycondensations (Flory, 1936; 1942) and on polyesters degradation (Flory, 1940; ref. 14 in Janmey, 1982, is misquoted). Thus, we could calculate the time-dependent conversion degree p_t as

$$p_t = \frac{(2[\alpha_2]_t + [A\alpha_2]_t)}{2[F_0]}, \qquad (13)$$

whereas the weight-fractions $w_i(p_t)$ were then calculated as

$$w_1(p_t) = \frac{[A_2\alpha_2]_t}{[F_0]} \quad \text{for the monomer} \qquad (14)$$

$$w_i(p_t) = \frac{0.5[A\alpha_2]_t}{[F_0]}\, i r_t^{(i-2)}(1-r_t) \quad \text{for } i \geq 2 \qquad (15)$$

with

$$r_t = \frac{2[\alpha_2]_t}{(2[\alpha_2]_t + [A\alpha_2]_t)}. \qquad (16)$$

If the solution is so dilute that the particles are not interacting, the intensity scattered by the overall sample can be expressed by Eq. 1, where $P_i(\theta)$ is the form factor of the ith polymeric chain of mass $M_i = iM_0$. Four different polycondensation polymers models were considered: rod-like, either end-to-end single-stranded (RLSS) or half-staggered double-

stranded (RLDS) stiff chains; and worm-like, either end-to-end single-stranded (WLSS) or half-staggered double-stranded (WLDS) semiflexible chains. For each of the four models M_w is the same and can be easily calculated at any p value by using Eq. 5 and Eqs. 8 or 14–16, whereas R_θ and $\langle R_g^2\rangle_z$ differ from model to model and can be determined after $P_i(\theta)$ and the radius of gyration $R_g(i)$ of the ith polymer are known. These were computed as follows.

The RLSS polymers were considered to be circular cylinders of length $L_i = iL_0$ and diameter d equal to the monomer diameter d_0. Thus, $P_i(\theta)$ was simply given by Eq. 2 and

$$R_g^2(i) = \frac{L_i^2}{12} + \frac{d^2}{8}. \tag{17}$$

The RLDS polymers were considered to be a rigid assembly of monomers aligned according to the well known half-staggered geometry (Ferry, 1952; Hall and Slayter, 1959), each monomer being a cylinder of length L_0 and diameter d_0. Because the relative distances among monomers are fixed (and known), $R_g(i)$ can be calculated by using standard formulas, and it is straightforward to show that

$$R_g^2(i) = R_g^2(0) + \frac{1}{2i^2}\sum_{k,m}^{i} r_{ij}^2, \tag{18}$$

where $R_g^2(0)$ is the square radius of gyration of the monomer (calculated with Eq. 17), and r_{ij} is the distance between the monomers centers of mass. As to $P_i(\theta)$, the ith polymer was assimilated to a rod of diameter d_i and length L_i so that its radius of gyration (calculated according to Eq. 17) is equal to that given by Eq. 18 and its molecular weight is equal to the expected value $M_i = iM_0$. This approximation might be rather rough for the first oligomers, but works fairly well as soon as the polymers start to grow, with the values of d_i and L_i, which asymptotically tend to $d_i = \sqrt{2}d_0$ and $L_i = (i/2)L_0$, respectively.

For most of the WLSS polymers, for reasons that will be explained in the Results section, the length L_m of the fibrin monomer units inside the polymers was considered to be different from that of the nonactivated, rod-like fibrinogen monomers. It was assumed to be $L_m = 75$ nm, and, to conserve the monomer volume, its diameter was fixed at $d_m = 2.45$ nm. The contour length of the ith chain was $L_c(i) = iL_m$ (for $i > 1$) and $L_c(1) = L_0 = 50$ nm for the monomer. The persistence length of the chain was set to be equal to the monomer length ($l_p = 75$ nm), or twice this value ($l_p = 150$ nm), regardless of $L_c(i)$. Only in one particular case, all the units were considered as for the RLSS case, with $L_0 = L_m = l_p = 50$ nm. Thus, $P_i(\theta)$ was calculated according to Eq. 3, whereas $R_g(i)$ was calculated from (Benoit and Doty, 1953),

$$\langle R_g^2(i)\rangle = L_c(i)\frac{l_p}{3}\{1 - 3\beta_i[1 - 2\beta_i + 2\beta_i^2 - 2\beta_i^2 e^{-(1/\beta_i)}]\}, \tag{19}$$

where $\beta_i = l_p/L_c(i)$. Note that, as for Eq. 3, when $\beta_i \gg 1$, the chain behaves as a rigid rod, and Eq. 19 reduces to the formula of an infinitely thin rod, $R_g^2(i) = (L_i^2/12)$.

Finally, the WLDS polymers were considered to be semiflexible chains obtained by assembling monomers of length L_0 and diameter d_0 according to the same half-staggered geometry used for the RLDS model. The ith polymer was characterized by a contour length $L_c(i)$ and a diameter d_i, which were determined by supposing that the polymer is infinitely stiff, and then by using the same procedure of the RLDS model. The persistence length l_p was taken to be equal for all the polymers, and values between 50 and 200 nm were chosen. For the WLDS model, the form factor $P_i(\theta)$ and radius of gyration $R_g(i)$ were calculated by using Eq. 3 and Eq. 19, respectively.

Thus, using Eqs. 1–3, 5, 6, 8–19, we have generated various R_θ data sets for the 15 different scattering angle values associated with the detectors of the MALLS photometer. Some discrete values between 0.01 and 0.6 for the degree of conversion p were chosen, and the sample concentration was assumed to be 0.33 mg/ml, corresponding to one of our experimental conditions. In generating the distributions, a cut-off value of 1×10^{-4} was used for $w_i(p)$, to reasonably limit the number of polymers present contributing to the scattered light intensity. Then, both statistical and systematic noise were added to the data. As mentioned in the previous section, the statistical noise was estimated from the fluctuations of the baseline signals provided by the buffer solution before injecting the sample in the cell. These fluctuations were found to be of the order of 1.5×10^{-7} cm^{-1} for the detectors at the lower two angles and the one at the largest angle. In between, they were somewhat smaller, of the order of 5×10^{-8} cm^{-1}. These values correspond to ~1% rms fluctuations of the intensity scattered by the buffer, which, in turn, is ~10-fold lower than the intensity scattered by the fibrinogen monomers (at the above-reported concentration) before polymerization is induced. Superimposed to the statistical noise, a little amount of systematic noise could also be added to the data for all the angles. Its level was chosen to be different from angle to angle, with the first and last ones being noisier because they are most susceptible to normalization errors, misalignments, and sensitive to stray light. For these two angles, the rms level was set equal to +0.5% of the signal level, whereas, for all the remaining angles, it was set to a relative value of 0.05%, with alternating positive and negative values.

Finally, for each polymerization model, fine-spaced sets of M_w and $\langle R_g^2\rangle_z$ data were generated by varying p in the range 0–0.9. These data were analyzed as $\langle R_g^2\rangle_z$ versus M_w plots and compared with the corresponding graphs obtained from the experimental data.

RESULTS

Basic performance of the stopped-flow MALLS set-up

In Fig. 4 are reported, as a function of time, the normalized raw scattering intensities, collected by the photodiodes placed at the various scattering angles, of a fibrin polymerization reaction ($c = 0.11$ mg ml^{-1}) initiated by thrombin with stopped-flow mixing and allowed to proceed until saturation of the lower angles detectors (only the first 1200 s are shown). As can be seen, the traces are quite smooth even at the lowest angle collected, ~22° (no mathematical smoothing was applied). In the inset, the fibrinogen "baseline" (negative time points) and the first 40 s after thrombin addition are highlighted on an expanded scale, to show the behavior at the very early stages. The sudden increase of noise on the lowest angle detector (*inset*, *upper trace*) appearing at −25 s happened occasionally due to the opening of the valves in preparation for injection of the fibrinogen/thrombin mixture. It can be also observed that, after only 5–7 s of polymerization, there is already a small but appreciable change in the intensity of scattered light from the value of the unreacted fibrinogen zone. Overall, these traces are indicative of the performance of the set up, especially for what concerns dust contamination and instabilities due to the stopped-flow mixing, and clearly show that, even at such low protein concentrations, it is possible to recover good data points with a 0.25-s time resolution.

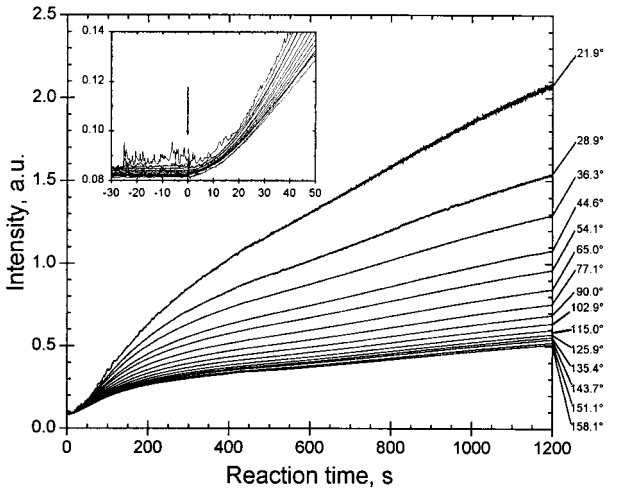

FIGURE 4 Plot of the scattered intensities as a function of time collected by the fifteen detectors of the DAWN-DSP-F photometer for the polymerization of fibrinogen (c = 0.11 mg ml^{-1}) induced by thrombin (0.25 nominal NIH units/mg FG). On the right y-axis are indicated the scattering angles seen by each detector. In the inset, the scattered intensities collected in the time range from 30 s before to 50 s after the injection of the reaction mixture (*vertical arrow*) are shown; the traces at negative times are due to the scattering of unreacted fibrinogen.

Next, we turned our attention to the problem of photodiodes normalization, to correct for their different responses. Whereas small errors in this procedure can be tolerated when dealing with either chromatograms or batch measurements on nonevolving samples, this was found not to be the case for polymerization studies. In particular, considering the peculiarities of the fibrinogen–fibrin conversion (see below), it was crucial to perform this operation as carefully as possible. To begin with, every batch of fibrinogen used in the polymerization studies was also analyzed by SE-HPLC with MALLS detection, as described for BSA in the Materials and Methods section, and using BSA for normalization. We consistently found an $(\langle R_g^2\rangle_z)^{1/2}$ of ~15 nm across the peak corresponding to monomeric fibrinogen (Bernocco, 1998), as will be reported in more detail elsewhere (Bernocco S., C. Cuniberti, and M. Rocco, in preparation). Incidentally, this $(\langle R_g^2\rangle_z)^{1/2}$ value compares well with the 14.2 ± 0.5-nm value obtained by small-angle x-ray scattering on bovine fibrinogen solutions (Lederer, 1972). Next, the BSA normalization obtained from SE-HPLC was introduced in the stopped-flow data files, but the results were uneven. Therefore, the stopped-flow data files were renormalized using the unreacted fibrinogen zone, using the 15-nm $(\langle R_g^2\rangle_z)^{1/2}$ value derived from the SE-HPLC separations. When checked against the original BSA normalization coefficients, the new coefficients were within 1% of the original values for angles above 40°, whereas changes of up to 5% were observed for the three lower angles. However, the improvement in the quality of data for the polymerization runs was quite good, especially on the early stages (data not shown). At longer times, when the scattering intensity had already risen by a factor of ten, the two normalizations performed similarly. Although this procedure can be questioned on an absolute scale, we feel that it can be justified at least from the point of view of the internal consistency of each data file. It is possible that, at these low macromolecular concentrations, small, flow-resistant spots in the cell borehole play a relevant role, especially at low scattering angles.

Stopped-flow MALLS data processing and evaluation

Experimental Zimm and Casassa plots

In Fig. 5, a series of snapshots taken at four different times during the polymerization of a fibrinogen/thrombin mixture at an initial FG concentration of 0.33 mg ml^{-1} are reported as Zimm-like plots (Fig. 5, *A–D*) or Casassa plots (Fig. 5, *E–H*). It is immediately evident that, already by 20 s after mixing (Fig. 5 *B*), roughly corresponding to a steep increase of the intensity registered by all the detectors (see Fig. 4), the Zimm plots are starting to deviate appreciably from linearity. The solid lines in Fig. 5, *A–D* are third degree polynomial fittings, whereas the dotted lines are linear regressions through all the data points (Fig. 5, *A–B*), or only through the first three data points (Fig. 5, *C–D*). The corresponding extrapolated M_w and $(\langle R_g^2\rangle_z)^{1/2}$ data are shown in Table 1. It must be pointed out that, although the third degree polynomials seems to nicely fit the data, the extrapolation of data from curved Zimm-plots is a potentially dangerous procedure (for instance, see Wiltzius et al., 1982a). Therefore, before further analyzing the whole set of experimental data, we performed a careful check of polynomial fitting using computed data (see next subsection below). Anyway, one may notice that the M_w recovered after 3 s (~330,000 g mol^{-1}, see Table 1) appears to be smaller than the expected value deduced from the amino acid sequence of FG, 340,000 g mol^{-1}. It is, however, already ~6% higher than the M_w value systematically recovered from the unreacted FG baseline (~310,000 ± 7000 g mol^{-1}, data not shown). This baseline value compares very favorably with the 307,000-g mol^{-1} M_w value calculated for our samples from the relative abundance of species containing α-chains partially degraded to various extents at their C-terminal ends, as described in Materials and Methods. In any case, it is probably unlikely that the overall polymerization process would be much affected by this relatively low degradation level.

In contrast to the Zimm plots, the Casassa plots (Fig. 5, *E–H*) show a remarkable degree of linearity, even at the shortest time considered, when the reacting mixture should still be dominated by the monomers (Fig. 5 *E*, 3 s). This is striking if one considers that, for the incident wavelength and the scattering angles used by us, the product qL_c for

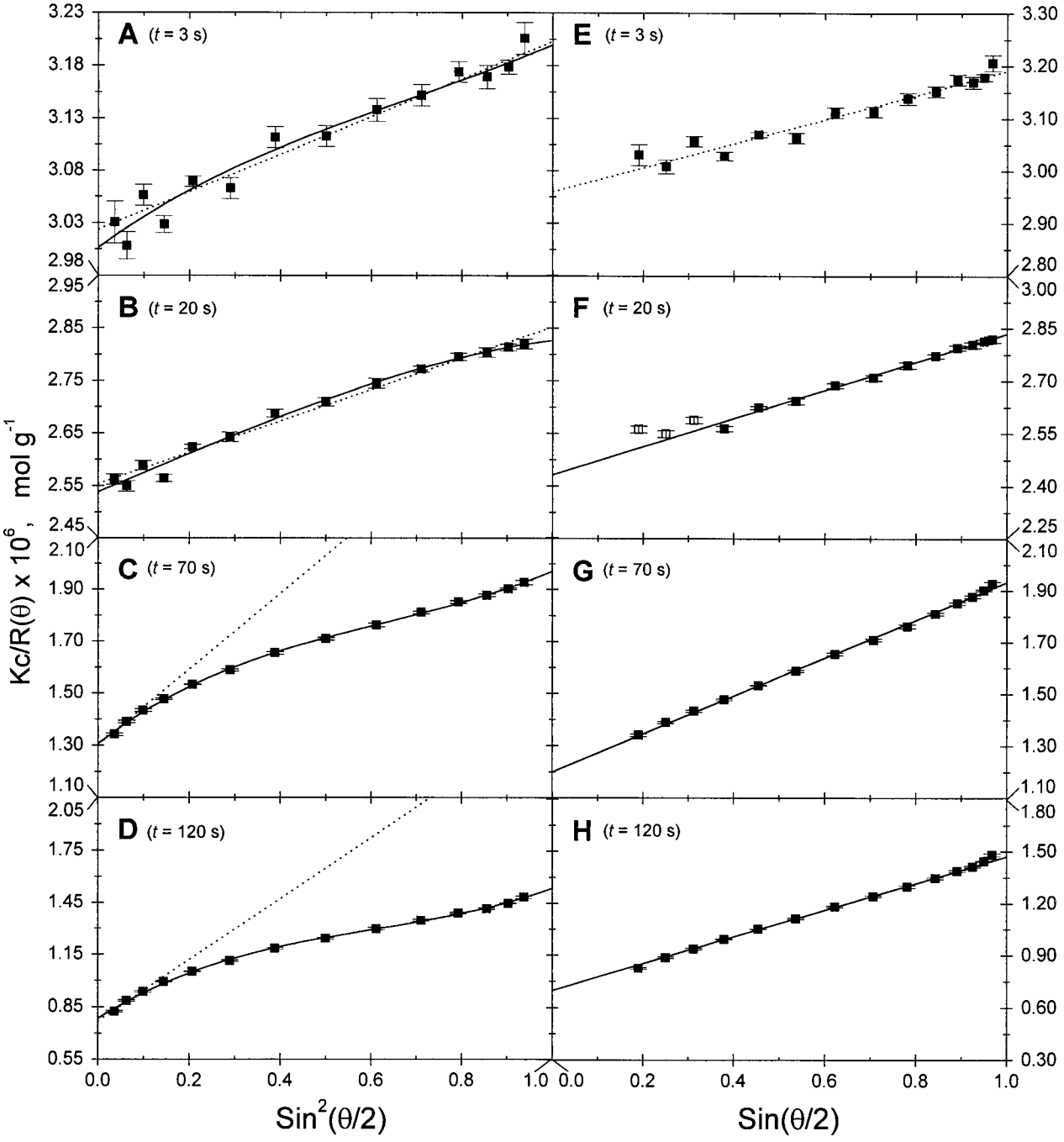

FIGURE 5 (*A–D*) Experimental Zimm and (*E–H*) Casassa plots obtained for the polymerization of fibrinogen ($c = 0.33$ mg ml^{-1}) induced by thrombin (0.25 nominal NIH units/mg FG), taken at four different reaction times: (*A*, *E*) 3 s; (*B*, *F*) 20 s; (*C*, *G*) 70 s; and (*D*, *H*) 120 s. (*A–D*) The continuous lines are third degree polynomial fittings, whereas the dotted lines are linear fittings through all the data points (*A* and *B*) or through only the first three data points (*C* and *D*). (*E–H*) The continuous lines are linear fittings and the open symbols denote the points not included in the regression.

monomeric FG is located between 0.25 and 1.3, and thus the conditions for the linearity predicted by Eq. 7 ($qL_c > 3.8$) are clearly not met. Furthermore, if we examine the apparent M_L values extrapolated from the linear fittings of the data presented in Fig. 5, *E–H* (Table 1, last column), we find that the early values are clearly inconsistent with any possible mechanism for fibrin polymerization: considering that the M_L value for fibrin monomers in our samples should be between 6000 and 6800 g mol^{-1} nm^{-1} (300,000–340,000/50), a $M_L \approx 33{,}000$ would imply the formation of up to

TABLE 1 Parameters extrapolated from the different polynomial fittings of the Kc/R_θ versus $\sin^2(\theta/2)$ data and from the linear fittings of the Kc/R_θ versus $\sin(\theta/2)$ data presented in Fig. 5.

Reaction Time (s)	M_w ($g\ mol^{-1} \times 10^{-5}$) Polynomial Degree		$(\langle R_g^2 \rangle_z)^{1/2}$ (nm) Polynomial Degree		M_L ($g\ mol^{-1}\ nm^{-1} \times 10^{-3}$)
	3rd	1st	3rd	1st	
3	3.33 ± 0.02	3.31* ± 0.01	20.3 ± 5.0	15.9* ± 0.5	(36.5 ± 1.1)†
20	3.95 ± 0.02	3.91* ± 0.02	27.7 ± 2.2	22.3* ± 0.5	(20.7 ± 0.7)†
70	7.60 ± 0.02	7.72‡ ± 0.06	64.8 ± 2.6	69.2‡ ± 8.0	11.5 ± 0.1
120	12.61 ± 0.02	13.27‡ ± 0.06	92.9 ± 3.4	99.4‡ ± 6.1	10.5 ± 0.2

*Whole range fitting.
†Values not reliable (see text).
‡First three data points fitting only.

five-stranded polymers already 3 s after mixing, when the M_w is still close to that of the monomer. Moreover, the M_L value rapidly decays to that expected for three-stranded polymers after 20 s, whereas the M_w is instead increasing. However, the situation stabilizes between 90 and 120 s around an acceptable value of M_L, ~10,500 $g\ mol^{-1}\ nm^{-1}$, which, considering that a relevant portion of unreacted fibrinogen probably is still present at this stage, is reasonably close to the $M_L \approx 12{,}000$–$13{,}600\ g\ mol^{-1}\ nm^{-1}$ value expected for the classic double-stranded fibrin protofibrils. The interpretation of this odd behavior of the Casassa plots also required the aid of simulated data (see the last two subsections of this section).

Simulated Zimm-plots, tests of the polynomial fittings, and comparison with the experimental data

As described in detail in Data analysis and simulations in Material and Methods, we have considered polydisperse collections of rod-like or of worm-like particles, either end-to-end single-stranded (RLSS and WLSS) or half-staggered double-stranded (RLDS and WLDS). For the RLSS, RLDS, and WLDS polymers, the monomeric repeating unit, as well as the nonactivated monomer, are rods 50 nm long, a compromise between the length derived from our SE-HPLC/MALLS fibrinogen R_g determination (~52 nm) and the EM-derived length (46–48 nm). For the WLSS polymers, the length of the monomeric units inside the polymers, but not that of the unreacted monomers, was taken to be 75 nm, as deduced by Wiltzius et al. (1982a) on the basis of their light scattering study. The rationale for this choice is to give some consideration to the idea that FG polymerization may also proceed via interactions between the αC domains, giving rise to more elongated and flexible structures. Likewise, WLDS polymers were considered because FG main body may possess a certain degree of segmental flexibility. In these initial simulations, the persistence lengths of the WLSS and WLDS polymers were chosen to be equal to the length of one monomer units, 75 and 50 nm, respectively. Polymer distributions were obtained from two different bifunctional polycondensation models, and the corresponding scattering functions were then calculated.

In Fig. 6, *A–D*, are shown the synthetic Kc/R_θ versus $\sin^2(\theta/2)$ data (*squares*, WLSS; *circles*, RLSS; *triangles*, RLDS) for a bifunctional polymerization in which the size distribution is that predicted by the Flory theory (Eq. 8). Four different conversion degrees were chosen to closely match the M_w extrapolated from the data of Fig. 5 (see Table 1). Likewise, the synthetic Kc/R_θ versus $\sin^2(\theta/2)$ data shown in Fig. 6, *E–H* were generated according to the theory of Janmey (1982) (Eqs. 9–16). In this case, the two FPA on each FG molecule are supposedly released with different rates characterized by a ratio Q (see Eq. 10). We have chosen $Q = 16$, a value that was found to give results consistent with many experimental data (Bale et al., 1982; Janmey et al., 1983a), and the resulting distributions became much broader and skewed toward longer polymers. Different conversion degrees were then chosen, again with the aim of matching the experimental M_w extracted from the data presented in Fig. 5, *A–D* (see Table 1). In addition to the WLSS (*squares*), RLSS (*triangles*), and RLDS (*circles*) polymers, WLDS semiflexible polymers (*diamonds*) were also considered in this simulation. All the data shown in Fig. 6 have been generated with both statistical and systematic noise, and the linear fittings (*dotted lines*, *panels A and D*) and third degree polynomial fittings (*solid lines*, *all panels*) are superimposed.

To estimate what errors we may incur by using different fitting procedures, the random generation of noise was repeated several times, and the ratios between original (synthetic) and fitted parameters were calculated. In Table 2, only the data for the RLSS and WLSS polymers generated using the Flory size distribution are reported. Four p values were chosen, 0.01, 0.10, 0.30, and 0.60, different from, but closely related to, those of Fig. 6. To begin with, in all the situations examined, the M_w value is recovered with near 100% precision by the third degree polynomial fitting procedure (*first two rows*), whereas the linear fitting (*third and fourth row*) starts to underestimate it at $p > 0.3$ (cf. Fig. 6 *D*). This is a clear function of the distribution of lengths of

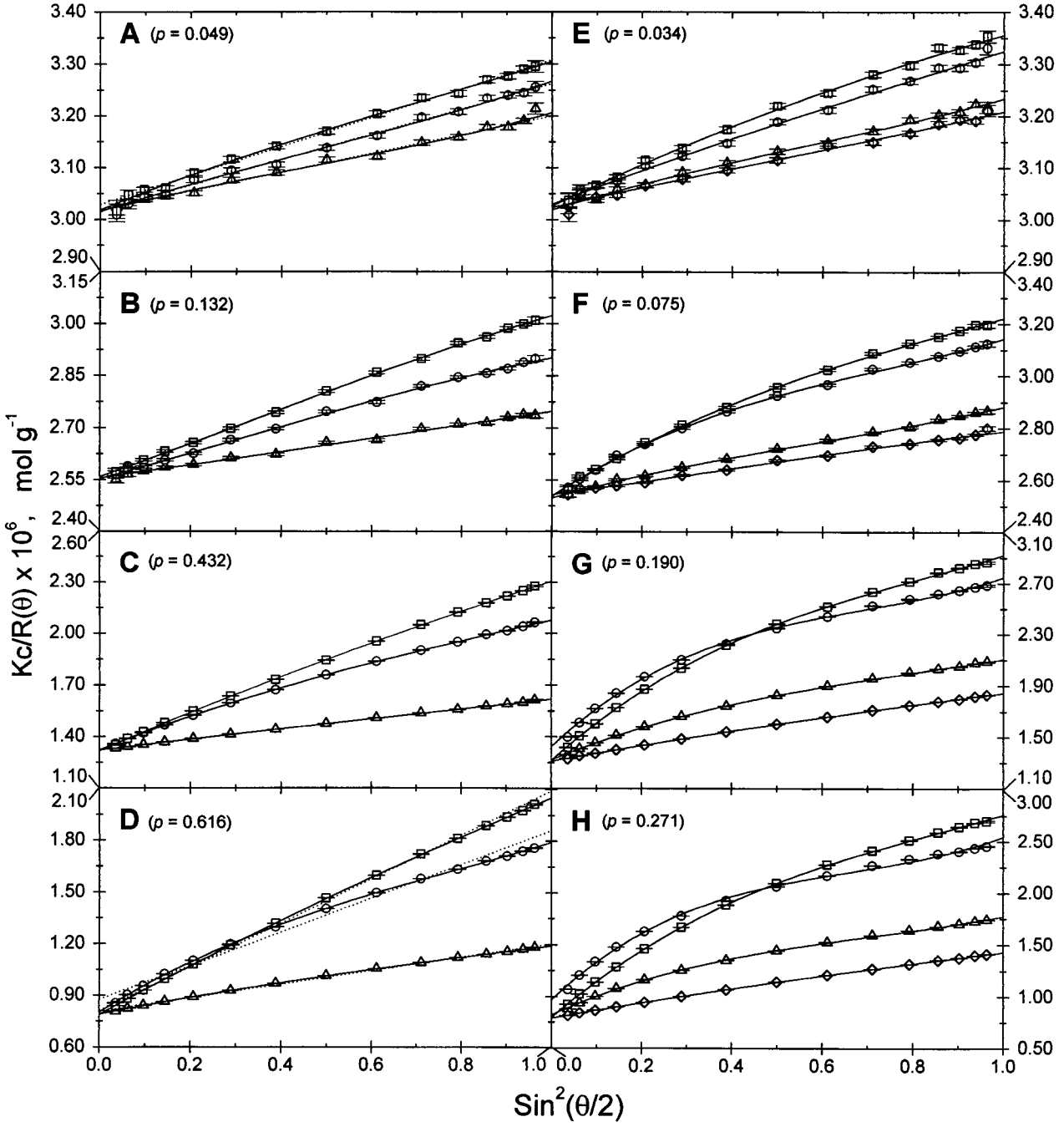

FIGURE 6 Calculated Zimm plots for polydisperse collections of polymers obtained from two different bifunctional polycondensations models. (*A–D*) Flory (Eq. 8); (*E–H*) Janmey with $Q = 16$ (Eqs. 9–16). The polymer models used correspond to: rod-like linear end-to-end single-stranded (RLSS, *circles*); rod-like half-staggered double-stranded (RLDS, *triangles*); worm-like linear end-to-end single-stranded with $L_m = l_p = 75$ nm (WLSS-75, *squares*); and worm-like half-staggered double-stranded with $L_0 = l_p = 50$ nm (WLDS-50, *diamonds*, *E–H* only). The continuous lines are third degree polynomial fittings, the dotted lines linear fittings. The conversion degree p is indicated in each panel.

the polymers in the mixtures, because, for the RLDS case, the M_w value is still recovered within 98% by a linear fitting even at $p = 0.6$ (data not shown).

For $\langle R_g^2 \rangle_z$, the situation is quite different (*fifth* to *fourteenth rows*). As could be expected, the major influence of the systematic noise added is felt at the lower p (*fourth* and *eighth columns*; cf. Fig. 6 *A*), where the solution composition is still dominated by the monomers. In this situation, the linear fitting gave the best results, but also the third degree polynomial recovered the input data within 2–20%,

TABLE 2 Ratios between recovered and theoretical (calculated) parameters for different kinds of fittings in the Kc/R_θ versus $\sin^2(\theta/2)$ plots for simulated data of polydisperse rod-like and worm-like polymers generated according to the Flory theory, with two different noise levels

Parameter	Polynomial fitting (detectors included)	Noise*	Rod-like single stranded (RLSS) polymers conversion degree				Worm-like single stranded (WLSS) polymers conversion degree			
			0.010	0.100	0.300	0.600	0.010	0.100	0.300	0.600
M_w	Third degree	Stat.	1.00 ± 0.00	1.00 ± 0.00	1.00 ± 0.00	0.99 ± 0.00	1.00 ± 0.00	1.00 ± 0.00	1.00 ± 0.00	0.99 ± 0.00
	(1–15)	Stat. & Syst.	1.00 ± 0.00	1.00 ± 0.00	1.00 ± 0.00	0.99 ± 0.00	1.00 ± 0.00	1.00 ± 0.00	1.00 ± 0.00	0.99 ± 0.00
M_w	First degree	Stat.	1.00 ± 0.00	1.00 ± 0.00	0.99 ± 0.00	0.91 ± 0.00	1.00 ± 0.00	1.00 ± 0.00	0.99 ± 0.00	0.91 ± 0.00
	(1–15)	Stat. & Syst.	1.00 ± 0.00	1.00 ± 0.00	0.99 ± 0.00	0.91 ± 0.00	1.00 ± 0.00	1.00 ± 0.00	0.99 ± 0.00	0.91 ± 0.00
$\langle R_g^2\rangle_z$	Third degree	Stat.	0.85 ± 0.26	1.02 ± 0.06	1.00 ± 0.02	0.92 ± 0.00	1.10 ± 0.15	1.03 ± 0.06	1.01 ± 0.02	1.00 ± 0.00
	(1–15)	Stat. & Syst.	0.98 ± 0.21	1.07 ± 0.06	1.02 ± 0.02	0.93 ± 0.00	1.19 ± 0.13	1.06 ± 0.05	1.02 ± 0.02	1.01 ± 0.00
$\langle R_g^2\rangle_z$	Third degree	Stat.	0.85 ± 0.25	1.02 ± 0.06	1.00 ± 0.02	0.91 ± 0.00	1.13 ± 0.16	1.02 ± 0.05	1.01 ± 0.02	0.99 ± 0.00
	(2–15)	Stat. & Syst.	0.91 ± 0.22	1.04 ± 0.06	1.01 ± 0.02	0.91 ± 0.00	1.17 ± 0.15	1.03 ± 0.04	1.01 ± 0.02	1.00 ± 0.00
$\langle R_g^2\rangle_z$	Third degree	Stat.	0.85 ± 0.25	1.01 ± 0.07	1.00 ± 0.02	0.92 ± 0.00	1.10 ± 0.12	1.03 ± 0.05	1.01 ± 0.02	1.00 ± 0.00
	(1–14)	Stat. & Syst.	0.96 ± 0.21	1.05 ± 0.07	1.00 ± 0.02	0.93 ± 0.00	1.17 ± 0.12	1.06 ± 0.05	1.02 ± 0.02	1.01 ± 0.00
$\langle R_g^2\rangle_z$	Third degree	Stat.	0.86 ± 0.24	1.01 ± 0.08	0.99 ± 0.03	0.91 ± 0.00	1.12 ± 0.14	1.02 ± 0.04	1.01 ± 0.02	1.00 ± 0.00
	(2–14)	Stat. & Syst.	0.88 ± 0.24	1.02 ± 0.08	1.00 ± 0.02	0.91 ± 0.00	1.14 ± 0.14	1.03 ± 0.04	1.01 ± 0.02	1.00 ± 0.00
$\langle R_g^2\rangle_z$	First degree	Stat.	1.00 ± 0.02	0.97 ± 0.01	0.89 ± 0.00	0.69 ± 0.00	0.99 ± 0.02	0.96 ± 0.01	0.94 ± 0.00	0.93 ± 0.00
	(1–15)	Stat. & Syst.	1.00 ± 0.02	0.97 ± 0.01	0.89 ± 0.00	0.69 ± 0.00	1.00 ± 0.02	0.96 ± 0.01	0.94 ± 0.00	0.93 ± 0.00

*Data are averages over several independent simulations of statistic noise (Stat.), to each one of which the same level of systematic noise (Syst.) was subsequently added.

albeit with a much greater uncertainty. However, the precision could be improved by removing some detectors from the fitting, a procedure that can be applied on real data when some points are clearly affected by spurious noise. It is also interesting that, at this low p, the $\langle R_g^2\rangle_z$ of the WLSS polymers was consistently overestimated, whereas for the RLSS polymers, it was underestimated and the uncertainty was greater.

As the reaction proceeds, we encounter a transition zone in which the two procedures perform equally well, corresponding to a conversion degree of ~0.1 (*fifth* and *ninth columns*; cf. Fig. 6 *B*), and, for higher conversion degrees, the advantages of using the polynomial fitting are quite evident. In the case of the RLSS polymers (*sixth* and *seventh columns*; cf. Fig. 6, *C* and *D*), $\langle R_g^2\rangle_z$ is recovered at worst within 8%, a value which is much better than the 30% underestimation for the linear fitting (see *last two rows*). For the WLSS polymers, it was already evident from the data in Fig. 6 *D*, that these polymers have a more linear behavior in the Zimm-plot in respect to the RLSS ones. Therefore, it does not come as a surprise that the $\langle R_g^2\rangle_z$ values are recovered extremely well by the third degree polynomial fitting procedure (*10th* and *11th columns*) and that the linear fitting also performs reasonably. It is also noteworthy that removing the two noisiest detectors (no. 1 and no. 15, 6th–12th rows) from the fittings yielded no particular statistically significant advantage in either case. As for the RLDS polymers, the $\langle R_g^2\rangle_z$ was recovered within 7% by the third degree polynomial fitting for the conversion degrees 0.01 and 0.1, and within 1% thereafter (data not shown).

However, the situation was sensibly different when the broader distributions predicted by the theory of Janmey were analyzed (Fig. 6, *E–H*). The lower p values in these panels for data sets having the same M_w as those of Fig. 6, *A–D*, reflect the skewness of this distribution toward higher molecular weights. In this case, we could consistently recover M_w and $\langle R_g^2\rangle_z$ only for the WLSS and WLDS polymers, with results comparable with those of Table 2, across the whole spectrum of p values examined (data not shown). When the rigid rod distributions were examined, the third degree polynomial performance quickly degraded as a function of the length of the species involved: for the RLSS polymers, errors of −8% and −32% for M_w and $\langle R_g^2\rangle_z$, respectively, were already obtained for the data shown in Fig. 6 *G* (*circles*), whereas, for the RLDS species (*triangles*), the errors were still within −1% and −8%, respectively, for the same set of data. At the highest p value examined ($p = 0.271$, Fig. 6 *H*), the RLDS M_w and $\langle R_g^2\rangle_z$ data were recovered within −4% and −17%, respectively. The situation could be somewhat improved by using a higher degree polynomial (a fourth degree reduced the error in M_w and $\langle R_g^2\rangle_z$ for the RLDS polymers at $p = 0.271$ to −2% and −10%, respectively), but a thorough examination of these inherently more unstable polynomials is outside the scope of this paper. The poorer performance of the third degree polynomial can be ascribed mainly to the contemporary presence of a large fraction of monomers having a small R_g together with a broad distribution of very long and stiff polymers. However, visual inspection of the Zimm plots built from experimental data, and the statistical indicators of the goodness of the polynomial fitting procedure, suggest that it is unlikely that we are dealing with such an extreme situation. For instance, compare the experimental Zimm plot on Fig. 5 *D*, with the RLSS and RLDS data in Fig. 6 *H* (*circles*, *triangles*, and relative *solid line* fits).

Based on these results, the whole spectrum of the experimental data was then processed with a third degree polynomial fitting, keeping in mind that, at the very beginning of the reaction, we may overestimate the $\langle R_g^2 \rangle_z$ value by as much as 20%, and underestimate it by a similar amount at the latest times examined. We have decided not to use a linear fitting for the earliest times, a third degree polynomial for the intermediate times, and a fourth degree polynomial thereafter, because it would have been difficult to establish without bias where to switch between the procedures, and because it would have led to a discontinuity in the extrapolated M_w and $\langle R_g^2 \rangle_z$ data sets (see below). As an additional check on the extrapolated data at the longer reaction times examined, we have fitted with a straight line the three lowest angles (see Fig. 5, *C–D*), on the assumption that, in this region, only the longest polymers would dominate the scattering. As can be seen in Table 1, this procedure gave results in reasonable agreement with the third degree polynomial fitting, albeit somewhat overestimated. For all these reasons, we cannot exclude that longer polymers were present, which would have been weighted in had we access to lower scattering angles. Therefore, the results derived from our experiments at the later times should be taken in a first approximation as a reasonable lower bound on the real polymer parameters.

Finally, something about the nature of the polymers and of their distribution can be inferred by comparing the experimental Zimm plot data with the whole set of simulated data, apart from those at the very early times where noise plays a major role. For instance, the curvature already present in Fig. 5 *B*, is better matched by the simulated data in Fig. 6 *F*, rather than the corresponding Fig. 6 *B*. In particular, the double-stranded simulations (*triangles* and *diamonds*) were more consistent with the experimental data, as evidenced by the same Kc/R_θ range spanned by these curves, 2.55–2.90 $\times 10^{-6}$. The same behavior is observed for the subsequent data points (Fig. 5, *C–D*), which are best matched by the simulated data for the double-stranded species presented in Fig. 6, *G–H*.

Simulated Casassa plots and comparison with the experimental data

The same simulated Kc/R_θ data of Fig. 6, but plotted against $\sin(\theta/2)$, according to Eq. 7 (Casassa plot), are reported in Fig. 7. By comparison with the experimental data of Fig. 5, *E–H*, it can be seen that their already-mentioned striking linearity is also at odds with the simulated data obtained with the classic Flory distribution of Eq. 8 (Fig. 7, *A–D*). In this case, the recovery of the correct M_L values for these polymer distributions, either rod-like or worm-like, single-stranded or double-stranded, can be reliably attained only at the highest conversion degree examined, ~0.6, and by including in the fitting only the last seven angles (see Fig. 7 *D*); actual ratios between calculated and fitted parameters not shown). Incidentally, for the WLSS polymers with $L_m = l_p = 75$ nm, the angular range where Eq. 7 is truly applicable, regardless of the lengths of the polymers in the distribution, would include only the last four angles. Conversely, the data obtained with the broader Janmey distribution (Fig. 7, *E–H*) show a higher degree of linearity. For instance, the single-stranded polymers simulated on Fig. 7 *F* (RLSS, *circles*; WLSS, *squares*) possess the linearity shown by the correspondent graph in Fig. 5, whereas the double-stranded counterparts (RLDS, *triangles*; WLDS, *diamonds*) do not. Again, this linearity is striking, considering the limits of applicability of Eq. 7. In any case, the Kc/R_θ range spanned by the double-stranded simulations is in better agreement with the experimental data, suggesting that, at these early stages, a mixture of single- and double-stranded structures may be present. As we go to the subsequent time snapshots, (Fig. 5, *F–G* and Fig. 7, *F–G*), relatively rigid double-stranded structures seem already to account for both the shape and the span of the experimental data. It must be pointed out that WLDS polymers with a very short l_p (50 nm), clearly always outside the range of applicability of Eq. 7, are shown here for reasons of clarity. For instance, at $p = 0.271$ more rigid structures with a $l_p = 200$ nm exhibit a linear Casassa plot across all the angles used here but the first two, and are almost superimposable on the RLDS points (data not shown).

The unexpected linearity of the simulated Casassa plots even when the polymers do not meet the conditions $qL_c > 3.8$ and $ql_p > 1.9$, may help to explain why unreasonably high M_L values were extrapolated from the experimental data up to a 70-s reaction time (see Table 1, last column). When in a polydisperse solution of rod-like or worm-like particles, some obey the condition for the linearity of Eq. 7 and some do not, the resulting Casassa plots may be still linear, depending on the distribution, but the extrapolated M_L values may be grossly wrong. For instance, the simulated data of the WLDS polymers in Fig. 7 *F*, are reasonably linear from detector 5 (54°) to detector 14 (151°), although they should not be, because, at this conversion degree, the monomers are still the predominating species. Moreover, the deduced M_L is 23,400 g mol^{-1} nm^{-1}, whereas the input, synthetic distribution has a M_L of 6,500 g mol^{-1} nm^{-1}! A similar behavior was observed at low conversion degrees for all the models examined (data not shown), and strongly suggest that great care should be taken in the interpretation of apparently good Casassa plots when dealing with highly polydisperse samples.

Finally, it must be noted that, with the distributions predicted by Eqs. 9–16 with $Q = 16$, the M_L value at $p = 0.271$ for RLDS or WLDS polymers should be only 7,700 g mol^{-1} nm^{-1}, whereas the experimentally derived value is ~10,500 g mol^{-1} nm^{-1} (see Table 1). At this conversion level, the linear fit recovers fairly well the input M_L value for RLDS polymers (−1%) and for WLDS polymers with $l_p = 200$ nm (−4%; data not shown). Therefore, the above-reported discrepancy cannot be attributed to a flawed data

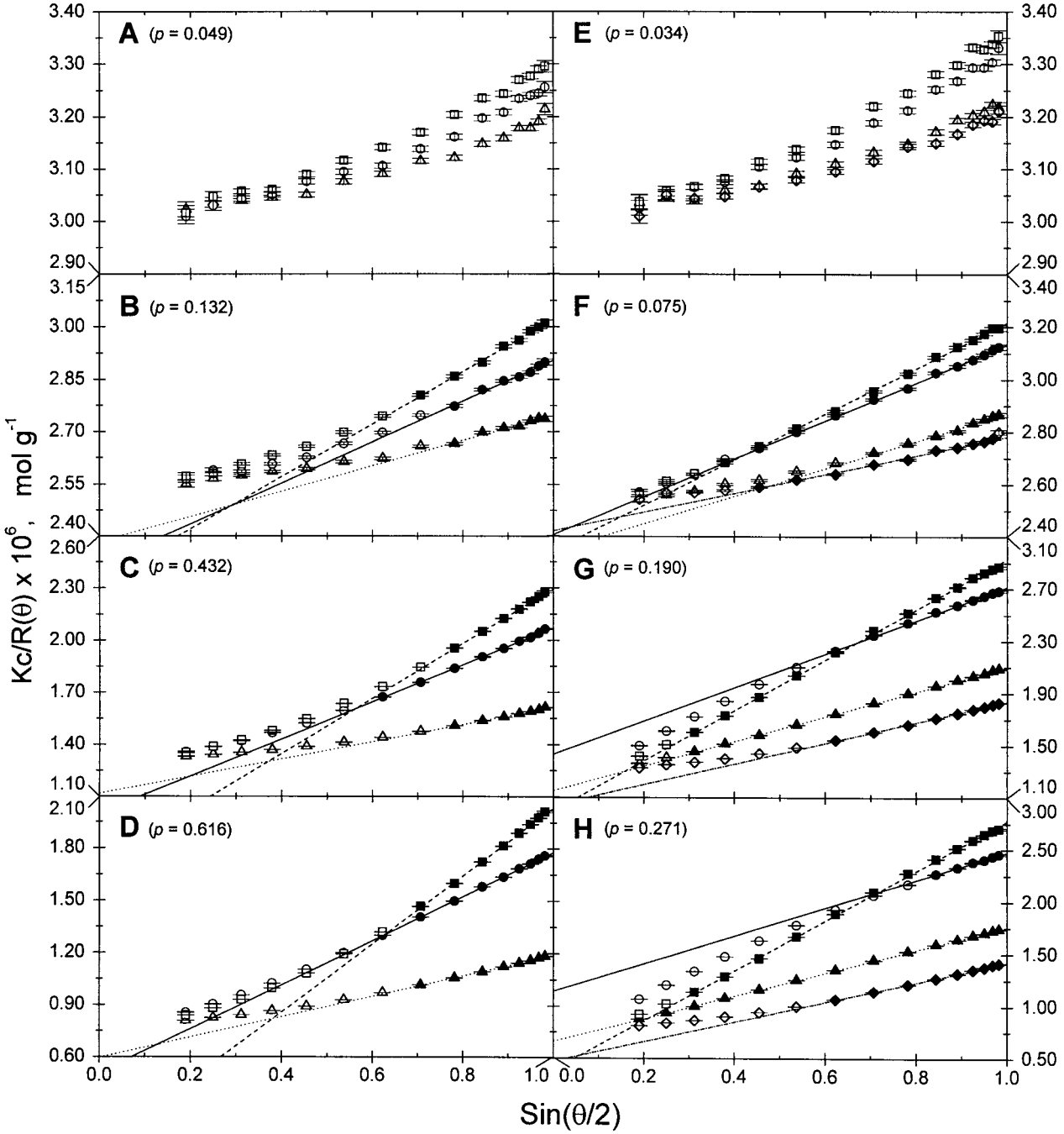

FIGURE 7 Calculated Casassa plots for polydisperse collections of polymers obtained from two different bifunctional polycondensations models. (*A–D*) Flory (Eq. 8); (*E–H*) Janmey with $Q = 16$ (Eqs. 9–16). Polymer models as in Fig. 6: RLSS (*circles*, *solid lines*); RLDS (*triangles*, *dotted lines*); WLSS-75 (*squares*, *dashed lines*); and WLDS-50 (*diamonds*, *dash-dot lines*, *E–H* only). The lines represent linear fittings, and the open symbols denote the points not included in the regression. The conversion degree p is indicated in each panel.

analysis and suggests that either the actual conversion degree might be larger than that predicted by Eqs. 9–16 with $Q = 16$, or a lower Q value has to be used. However, the latter case would also produce less linear Casassa plots, leaving this issue still open (see below).

A summary of the time-dependent data extracted from the experimental Zimm and Casassa plots

The whole data set for the first ~250 s, extracted from the Zimm and Casassa plots, for a thrombin-catalyzed fibrin

polymerization reaction at 0.33 mg ml^{-1} initial FG concentration, is presented in Fig. 8. By comparing Fig. 8 *A* with Fig. 8 *B*, it is immediately evident that, from ~60 to ~220 s, the M_w values grow linearly with time, whereas the $(\langle R_g^2\rangle_z)^{1/2}$ in this time interval enter a regime of nearly asymptotic growth, after an initial period of almost linear growth. Interestingly, this transition region encompasses the point (~90 s) at which the M_L (Fig. 8 *C*) stabilizes around the 10,500 g mol^{-1} nm^{-1} value still ~20% lower than that expected for a double-stranded fibril (see also Table 1), only slowly growing thereafter. Oddly, this behavior seems to indicate that, by this time, most of the FG has already been consumed, in contrast with the low conversion degree value deduced in the previous paragraphs. To better clarify this point, we have measured by reverse-phase HPLC the relative amounts of FPA and FPB as a function of reaction time. FG at 0.5 mg ml^{-1} was reacted with thrombin at 0.25 nominal NIH units/mg FG in TBS, conditions very close to those of the stopped-flow MALLS experiments. However, we found that thrombin became gradually less active when sitting in between polymerization runs in the glass syringe of the stopped-flow device. Because the data reported in Fig. 8 were extracted from the third run in a series, the experiment was performed after 1 h incubation of the enzyme in a glass syringe. A detailed description of the methodology (based on Kehl et al., 1981) and a complete set of data will be reported elsewhere, in a more comprehensive study of fibrinopeptides release under different solvent conditions (Profumo, A., S. Bernocco, G. Damonte, C. Cuniberti, and M. Rocco, in preparation). Here we would like to mention that, by 60 s, the FPA and FPB amounts are ~25% and ~2%, respectively, of their corresponding total amounts measured at the end of the reaction, in qualitative agreement with the low conversion degree deduced from the 70-s Zimm plot data. After 240 s, only ~61% of FPA and as much as ~12% of FPB have been released. Incidentally, the latter number may suggest that lateral aggregation between the double-stranded fibrils could have already started to take place, whereas the data derived from the Casassa plots (Fig. 8 *C*) still show only a slight increase in the M_L ratio. In any case, the FPA release data are also in contrast with the M_L data. A possible explanation for this apparent rapid depletion of monomeric, nonactivated FG from the solution, would involve its complexation with fibrin monomer, as proposed originally by Belitzer and Chodorova (1952) and subsequently studied in more detail by other workers (Shainoff and Page, 1962; Brass et al., 1976; Brosstad et al., 1979, and references therein). The complex(es) likely form because the complementary *a* sites, always available on the D domains of both FG and fibrin monomer, will compete for the *A* sites present only on the E domain of fibrin monomer, presumably forming mainly half-staggered mixed dimers and possibly even trimers. Unfortunately, the binding constant(s) for this complex(es) are not known to the best of our knowledge, rendering problematic a detailed simulation of this effect. However, a coarse simulation is presented in Fig. 8 *C*, where two curves are superimposed to the Casassa plot-derived data. The dotted curve corresponds to a M_L versus time simulation according to the Janmey theory (Eqs. 9–16) and a WLDS model, with [Th] = 0.05 NIH units ml^{-1} to roughly reproduce the experimental FPA release data. Still in the Janmey theory framework, the solid curve was instead obtained by imposing that both the monofunctional $[A\alpha_2]_t$ and the bifunctional $[\alpha_2]_t$ monomers are bonded to the nonactivated $[A_2\alpha_2]_t$ monomers. In this way, the weight fraction of all the monomers in solution is reduced, with respect to the value predicted by Eq. 14, by a quantity equal to $([A\alpha_2]_t + [\alpha_2]_t)/[F_0]$. Correspondingly, the weight fraction of the dimers is increased by the same quantity, while the weight fraction of all the other polymers

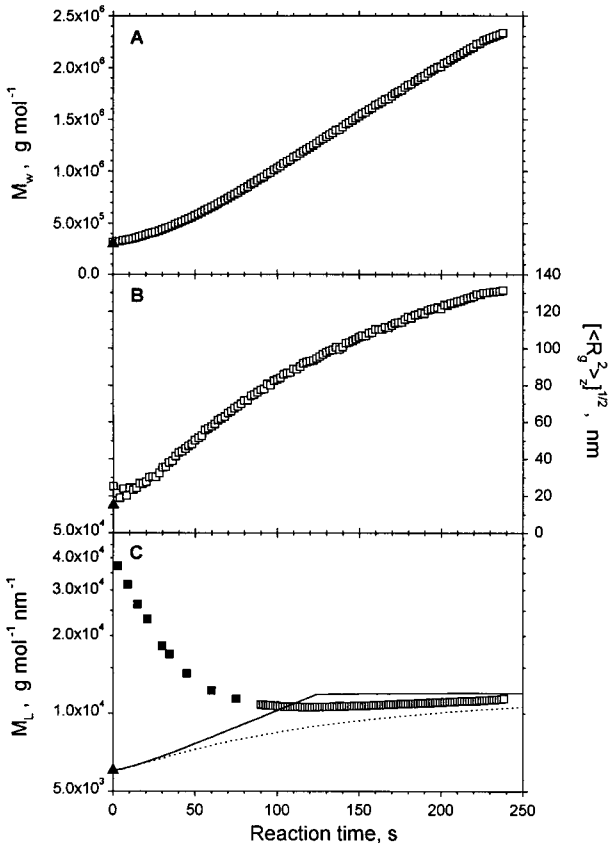

FIGURE 8 Plots of the values of (*A*) M_w and (*B*) $(\langle R_g^2\rangle_z)^{1/2}$, derived from Zimm-like plots, and of (*C*) M_L, derived from Casassa plots, as a function of reaction time for the thrombin-catalyzed fibrinogen polymerization. In every panel, the *filled triangles* represent the fibrinogen baseline values (0 s). For reasons of clarity, only ~¼ of the actual data points are shown in (*A*) and (*B*) (a point every 2 s). In (*C*), only few points have been calculated for the first ~90 seconds (*filled squares*), and thereafter ~⅙ of the calculated data points are shown (a point every 3 s; see text for details). Superimposed in (*C*) are the theoretical curves computed for a WLDS polymerization model according to Eqs. 9–16 (*dotted line*) or after introducing the contribution of the FG–fibrin monomer complex (*solid line*). Fibrinogen and thrombin concentrations as in Fig. 5.

is left unchanged. As can be seen, the curve obtained with the modified form of Eqs. 14–15 (*solid curve*) reaches the expected M_L plateau more rapidly than the corresponding curve obtained from the unmodified equations (*dotted curve*), while the experimental data lie in between. However, it cannot be excluded that single-stranded species could also contribute to these lower than expected M_L values. At the same time, these data would seem to downplay the onset of branching as an explanation for the nonlinear growth of $(\langle R_g^2\rangle_z)^{1/2}$ in this region.

Comparing extrapolated parameters with model curves

Additional valuable information can be gained by plotting on a double logarithmic scale $\langle R_g^2\rangle_z$ versus M_w, as used originally by Müller and Burchard (1978; Müller et al., 1981). In Fig. 9, such plots (*open squares with vertical error bars*) are presented for two starting FG concentrations, 0.33 mg ml^{-1} (Fig. 9, *A* and *B*) and 0.11 mg ml^{-1} (Fig. 9 *C*), both at the same nominal FG/thrombin ratio. In the insets (Fig. 9, *D–F*), the values of $\langle R_g^2\rangle_z$ versus M_w obtained during the first ~40 s of the reaction are reported on an expanded scale (*points connected by a continuous line*). It must be pointed out that, in these plots, the time dependence of the M_w and $\langle R_g^2\rangle_z$ data is removed, allowing the direct comparison between runs proceeding at different velocities. However, some indicative time points are overlaid on the plots, marked by the arrows (the first four time points in Fig. 9, *A–B* correspond to those of Fig. 5, *A–D* and *E–H*). The apparent discrepancy between the data in Fig. 9, *A–B* and that in Fig. 9 *C*, as the reaction at lower fibrinogen concentration (Fig. 9 *C*) seems to proceed faster, is due to the gradual inactivation of thrombin in the glass syringe of the stopped-flow device (see the previous section, A summary of the time-dependent data). The data presented in Fig. 9 *C*, were derived from an experiment in which the reaction was started immediately, whereas those in Fig. 9, *A–B* were recorded as the third run in a series: as can be seen, this inactivation notwithstanding, the reproducibility is good. Because we were not concerned in this study with the effects of different enzyme:substrate ratios, no attempt was made to determine the real thrombin activity.

Superimposed on the plots in Fig. 9, *A* and *B*, and in their relative insets *D* and *E*, are some theoretical curves derived from the bifunctional polycondensation models described in Materials and Methods (Data analysis and simulations), and already used in the previous sections. In Fig. 9 *A* and *D*, the curves are obtained with the Flory most probable distribution (Eq. 8), and correspond to RLSS, RLDS, WLSS-75, and WLSS-150 polymers (see the figure legend for the details). In Fig. 9 *B* and *E* the curves are obtained according to the theory of Janmey (1982) (Eqs. 9–16), with the ratio $Q = 16$ (see Eq. 10). To avoid confusion, the curves in Fig. 9 *B* were also labeled with the Q value (RLDSQ16, WLSSQ16-50, and WLSSQ16-75). WLDS polymers were also considered (WLDSQ16-50 and WLDSQ16-200), whereas the RLSS were omitted here because they produced curves clearly outside the range of the experimental data, and were replaced with a RLDS simulation with $Q = 32$ (RLDSQ32). For clarity, in Fig. 9, inset *E*, only three model curves are reported. Finally, we have also added in Fig. 9 the expected $\langle R_g^2\rangle_z$ versus M_w values deduced from the double-stranded polymers distributions measured by Weisel (Fig. 3 *C* of Weisel et al., 1993), according to an RLDS (panel *A*, *filled squares*) and a WLDS with $l_p = 200$ nm (panel *B*, *filled diamonds*) models. These distributions were obtained at three different reaction times from electron micrographs of a thrombin-induced fibrin polymerization (Weisel et al., 1993), although their experimental conditions were quite different from ours (similar ionic strength and pH, but 0.1 mM $CaCl_2$ instead of 1 mM EDTA-Na_2, and a non rate-limiting thrombin/FG ratio).

As can be seen from the data in Fig. 9 *A* (Flory distributions), the RLDS model does not fit the experimental data from the beginning of the reaction up to M_w values of more than 3×10^6 g mol^{-1}. It is of note that this simulation is roughly compatible with the points calculated from Weisel's EM data (*filled squares*), although it diverges for M_w values above 3×10^6 g mol^{-1}. Instead, both the single stranded polymerization models, (RLSS) (with monomer length of 50 nm), or WLSS-75 (with activated monomer length and persistence length both of 75 nm), seem to fit the data sets pretty well up to M_w and $\langle R_g^2\rangle_z$ values of ~800,000 g mol^{-1} and $\sim 5 \times 10^3$ nm^2, respectively, after which only the WLSS-75 model seems to apply (see also Fig. 9 *D*). However, by comparing these data with those presented in Fig. 8 *C*, derived from the same experiment, one can see that, by the time the M_w has reached a value of ~800,000 g mol^{-1}, the M_L values have almost decayed to the 10,000–11,000 g mol^{-1} nm^{-1} value clearly incompatible with a pure single-stranded model.

The rigid double-stranded model seems to fail also when the Janmey distribution with $Q = 16$ was simulated, as can be seen in Fig. 9 *B* (RLDSQ16). In fact, this model appears to fit very well in the initial stages up to ~70 s (see also Fig. 9 *E*), but cannot explain the later behavior of the $\langle R_g^2\rangle_z$ versus M_w curve. Higher values of Q, suggested in a subsequent EM-based study (Janmey et al., 1983b), are even more incompatible with our experimental data, as evidenced by the RLDSQ32 curve in Fig. 9 *B*, obtained for $Q = 32$. Again, a WLSS model with a short l_p (WLSSQ16-50, with both $L_0 = l_p = 50$ nm) provides an excellent fit to the experimental data, but, as for the WLSS-75 model in Fig. 9 *A*, it is also incompatible with the Casassa plot results. Double-stranded worm-like models were then tried, and indeed a simulation with $l_p = 200$ nm (WLDSQ16-200) reasonably matches the experimental data at least up to 120 s. However, the predicted M_L value for this kind of

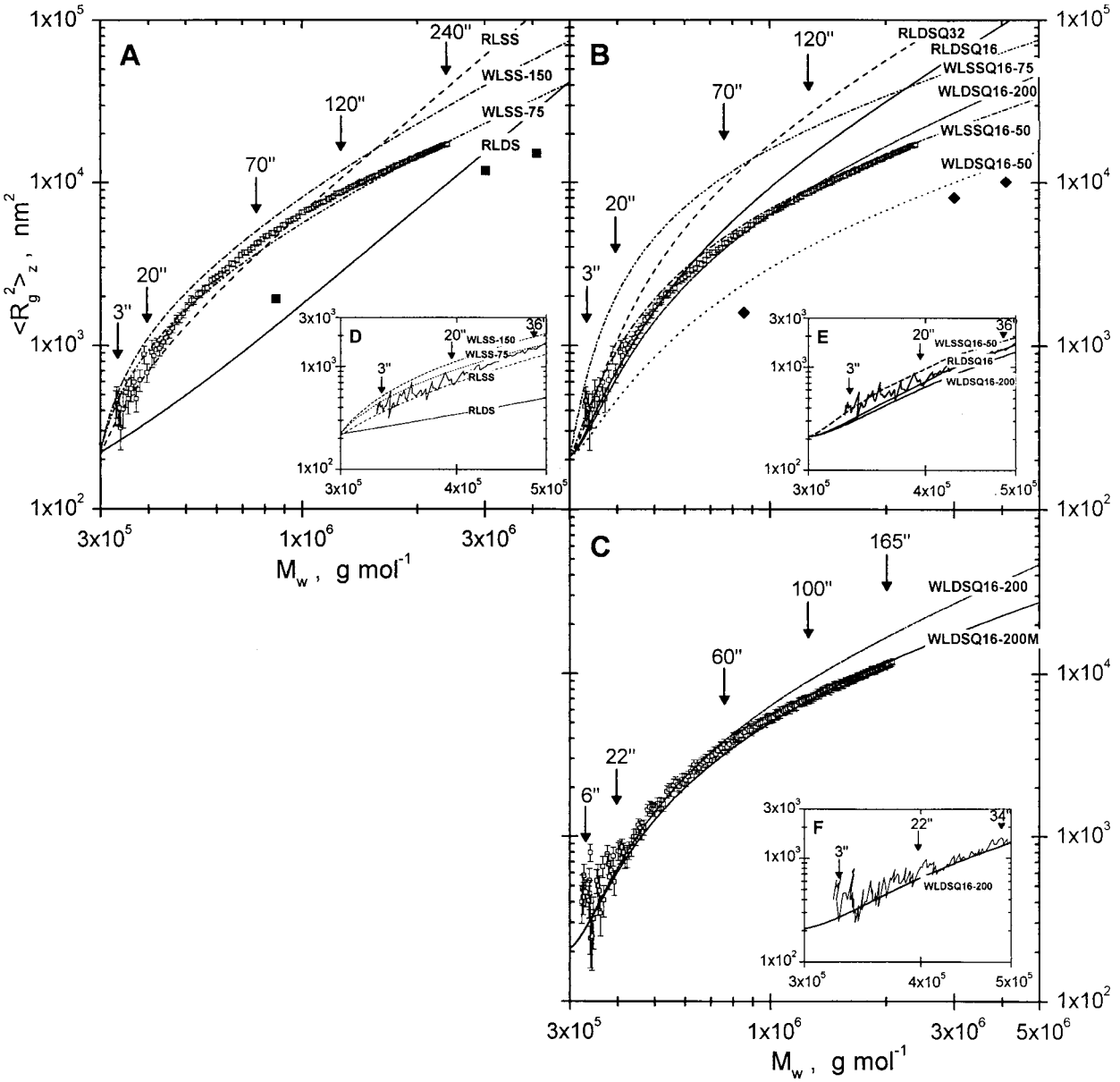

FIGURE 9 Double logarithmic plots of $\langle R_g^2 \rangle_z$ versus M_w, for two different data sets (*A–B*), fibrinogen $c = 0.33$ mg ml^{-1}; (*C*) $c = 0.11$ mg ml^{-1}; thrombin 0.25 nominal NIH units/mg FG in all panels). The computed standard deviations on the $\langle R_g^2 \rangle_z$ values are shown as vertical error bars (the corresponding error bars on M_w are smaller than the points size). Data in *A–B and in C* were collected at 0.5 s and 0.25 s intervals, respectively, but only a point every 1.5 s and every 0.75 s, respectively, are shown for reasons of clarity. Superimposed and labeled are the theoretical curves calculated for different bifunctional polycondensations models [(*A*) Flory distribution; (*B–C*) Janmey distribution with $Q = 16$ or $Q = 32$] of rod-like monomers with different polymer geometries: RLSS (*dashed line*); RDLS and RLDSQ16 (*continuous lines*); RLDSQ32 (*dashed line*); WLSS with $L_m = 75$ nm and either $l_p = 75$ nm (WLSS-75 and WLSSQ16-75, *dash-dot-dot lines*), or $l_p = 150$ nm (WLSS-150, *dash-dot line*), or with $L_0 = l_p = 50$ nm (WLSSQ16-50, *dash-dot line*); WLDS with $L_0 = 50$ nm and either $l_p = 50$ nm (WLDSQ16-50, *dotted line*) or $l_p = 200$ nm (WLDSQ16-200, *short dash-dot-dot line*). Some indicative time points are also indicated (*arrows*). The WLDSQ16-200M curve (*solid line*) shown only in (*C*) is similar to the WLDSQ16-200 but includes the contribution of FG–fibrin monomer complexes. In the insets (*D–F*), the data collected during the first ~40 s of the reactions are shown on an expanded scale, as points connected by a continuous line (the error bars have been omitted for clarity); some theoretical curves are also shown as in (*A–C*).

polymers at these conversion degrees is ~7700 g mol^{-1} nm^{-1}, still ~20% lower than those reported in Fig. 8 *C*. A worm-like double-stranded simulation with a persistence length equal to one monomeric unit (WLDSQ16-50) is also presented for comparison; oddly, it seems to almost follow the electron micrographs-derived values (*filled diamonds*), which were, however, calculated in this case for a $l_p = 200$ nm.

The WLDSQ16-200 curve is also replotted in Fig. 9, *C* and *F*, were the $\langle R_g^2 \rangle_z$ versus M_w values for a fibrin polymerization at c = 0.11 mg ml^{-1} are reported. Good reproducibility was obtained up to 60 s, with an earlier departure from the experimentally derived data in respect to those of Fig. 9 *B*. However, it must be mentioned that the data in Fig. 9 *C* were obtained after discarding the signal from the lower angle detector, which were of poor quality, and therefore the $\langle R_g^2 \rangle_z$ values for M_w values above 1×10^6 g mol^{-1} could be even more underestimated than the corresponding data in Fig. 9 *B*. The effect on the simulated curves of including the FG–fibrin monomer complex is also shown in Fig. 9 *C*, where a modified WLDS model with $l_p = 200$ nm is plotted (WLDSQ16-200M, *solid line*). As can be seen, an even better agreement is obtained, and, considering the roughness of the correction, this result strongly supports the notion that FG–fibrin monomer complexes do indeed form in the early stages of polymerization.

DISCUSSION AND CONCLUSIONS

Performance of the stopped-flow MALLS set-up and data analysis

In this paper, we have described a set-up for performing stopped-flow MALLS experiments using commercially available instruments. Several experimental problems have been dealt with, the most notable being related to the normalization of the separate detectors used, and solutions have been proposed. Moreover, we have studied a particular polymerization, in which a macromolecular rod-like monomer forms elongated polymers polydisperse in both length and width in the early stages of the reaction. This yields curved Zimm-like plots already at relatively low conversion degrees, from which the parameter $\langle R_g^2 \rangle_z$ cannot be recovered by linear fitting. To overcome this limitation, and taking advantage of the multiangle detection, we have used a third degree polynomial fitting, and we have demonstrated that, if the size distribution is relatively narrow, this procedure can yield values at worst within 10–20% of the true ones for $\langle R_g^2 \rangle_z$ values from ~200 up to ~1×10^4 nm^2. These results are slightly dependent on the shape and stiffness of the polymers, with the greater uncertainties occurring, for different reasons, at the lower and at the higher end of the $\langle R_g^2 \rangle_z$ range, whereas much better results are always obtained for M_w. Unfortunately, if the distribution becomes broader and skewed toward the high molecular-weight species, the performance of the third degree polynomial fitting is severely affected when stiff polymers are involved, worsening as the gap between the monomer and the polymers lengths becomes wider. Whereas such a situation could be recognizable in practice by the particular shape of the Zimm plot and from the degraded statistical performance of the polynomial, great care should be exerted when the extrapolated $\langle R_g^2 \rangle_z$ values exceed 1×10^4 nm^2. Tests are in progress to ascertain the performance of higher-degree polynomials, which could further push this limit. However, it must be also mentioned that $\langle R_g^2 \rangle_z$ values of ~$1–2 \times 10^4$ nm^2 are, in any case, at the limit of those that can be measured with confidence without corrections for depolarizing effects: for instance, neglecting the depolarization contribution leads to an error of ~3% in the estimation of the R_g of tobacco mosaic virus, a rod-like particle whose length is ~300 nm (Geiduschek and Holtzer, 1958).

Our simulations have also provided insights into the behavior of the Casassa plots when highly skewed distributions of rod-like or worm-like polymers are present. In particular, it is found that the Casassa plot may appear linear even if the conditions for its applicability ($qL_c > 3.8$ and $ql_p > 1.9$) do not hold, potentially leading to large errors in the estimation of the M_L ratio. To be able to discern when the Casassa plot is reliable, one should combine the information derived from Zimm and Casassa plots with appropriate modeling procedures.

Application to the fibrinogen–fibrin conversion

The techniques described have been applied to study the thrombin-catalyzed FG–fibrin conversion, starting from where it was left more than fifteen years ago after the seminal works by Hantgan and Hermans (1979) and of the Burchard and Känzig–Straub groups (Müller and Burchard, 1978; Müller et al., 1981; Wiltzius et al., 1982a,b), taking advantage of the notable increase in time resolution and statistical accuracy afforded by our stopped-flow MALLS set-up. This has allowed us to recover M_w and $\langle R_g^2 \rangle_z$ values for polymerizing solution of fibrinogen following its conversion to monomeric fibrin by relatively high, but still rate-limiting, amounts of thrombin, with a time resolution of ~0.25 s. Although our experimental conditions are quite different from those used by all the previously mentioned authors, it is of interest to compare some of the results we have obtained with theirs, and then draw our conclusions. We will begin with a review of the polymerization schemes and polymer models used, followed by a more in-depth analysis of our data.

Polymerization schemes

First of all, both Müller and Burchard and Wiltzius and coworkers have tried to model the whole process of fibrin formation, from the initial events to the gel point and beyond. To do so, they resorted to complicated polymerization models to account for linear aggregation, lateral aggregation, and branching. This is justified by the fact that fibrin monomer is at least tetrafunctional, although the second pair of interaction sites (B-*b*) do not seem to come into play until later on in the polymerization process under physiological conditions. Incidentally, it must be pointed out that even the $(\alpha B \beta \gamma)_2$ monomer can be considered bifunctional only in the half-staggered geometry, assuming that the interaction

between the two pairs of complementary A-*a* sites happens simultaneously. In any case, because we are concerned in this paper with early events in fibrin polymerization, we have elected to generate simulated data using only bifunctional polycondensation schemes. Although their full applicability can be questioned even for this shorter time frame (see below), some interesting conclusions can be drawn anyway from this type of modeling. Along this line, we felt that more detailed kinetic simulations, like those developed by Weisel and coworkers (Weisel and Nagaswami, 1992; Weisel et al., 1993), will become very useful after a wider set of data had been collected.

The two bifunctional polymerization schemes investigated here rely on different assumptions. The classic Flory polycondensation, leading to the polymer distribution described by Eq. 8, was used to describe the fibrin polymerization by Hantgan and Hermans (1979), who used very high thrombin/FG ratios (50–200 NIH units/mg FG) to make the assembly almost independent of the activation step. On the opposite side are the works of Janmey and Ferry (Nelb et al., 1980; Janmey, 1982; Bale et al., 1982; Janmey et al., 1983a), who first noted that, at much lower thrombin concentrations, the distribution of fibrin polymers, enzymatically crosslinked and separated by gel electrophoresis, appeared to be much more skewed toward high molecular-weight species than would be expected from the Flory theory (Nelb et al., 1980). Working on the hypothesis that the release of the FPA by thrombin is a nonrandom event, but that the second FPA on each FG molecule is released much faster than the first by a factor Q, Janmey developed a set of equations to calculate the polymer size distribution of such a reaction mixture (Janmey, 1982). To do so, he assumed that, at sufficiently low thrombin/FG ratios, the assembly would be much faster than the enzymatic step, and thus, at any given time, the size distribution could be approximated starting from the Flory theory, taking into account the simultaneous presence of mono- and bifunctional species (Janmey, 1982). Incidentally, for $Q = 1$, the Flory distribution is recovered, whereas as Q increases, less temporary monofunctional units are formed, and the distribution is effectively skewed toward longer oligomers. The theory was tested using thrombin/FG ratios $\leq$0.012 NIH units/mg FG, and good agreement was found with experimental data when $Q = 16$. This $Q = 16$ value was again found when light scattering data in the literature were analyzed, from which they concluded that either the monomers are at least tetrafunctional even before removal of the FPB, or indeed "the reaction between thrombin, fibrinogen, and fibrin oligomers produces disproportionately many difunctional monomers and so favors the growth of longer oligomers early in the reaction" (Janmey et al., 1983a). In later EM-based work, even higher values of Q were found to better match the experimental data (Janmey et al., 1983b).

Our experiments were done at a nominal thrombin/FG ratio, 0.25 NIH units/mg FG, which is an order of magnitude higher than, but still closer to that used by Janmey and collaborators (Bale et al., 1982), than to that used by Hantgan and Hermans (1979). Indeed, much better agreement with our experimental data was found when they were compared with polymerization models based on the theory of Janmey, as opposed to models based on the classic Flory theory. For instance, compare the shapes of the experimental Zimm and Casassa plots (Fig. 5, *A–D* and *E–H*, respectively) with the correspondent simulated data in Figs. 6–7 (panels *A–D*, Flory distributions; panels *E–H*, Janmey distributions with $Q = 16$). This finding is further strengthened by the recent publication of electrophoretic light scattering evidence for only the $(\alpha B\beta\gamma)_2$ fibrin monomer species (Li et al., 1996). However, our modeling points to a more complicated situation, as discussed below.

Polymers models

Whereas the works of Janmey and Ferry and of Hantgan and Hermans were mainly concerned with molecular weight distributions, we have also extracted from our data values for two shape-dependent parameters, the square average radius of gyration and the average mass per unit length. An estimation of these parameters was also provided by Müller and Burchard (Müller and Burchard, 1978; Müller et al., 1981), whereas Wiltzius et al. (1982a) initially refrained from the extrapolation of $\langle R_g^2\rangle_z$ from curved Zimm plots and reported only the M_L ratio together with a measure of the translational diffusion coefficient from dynamic light scattering data. In a subsequent study, Wiltzius et al. (1982b) used a special cell to extend the accessible scattering angles down to ~5.5°, recirculating the polymerizing solution in the first 3 min of reaction through a 0.3-μm filter to overcome the serious dust contamination problems at these low angles (a questionable procedure when dealing with evolving systems). Assuming linearity of the Zimm plots in this angular range, they provided a few $(\langle R_g^2\rangle_z)^{1/2}$ and M_w data points over the entire process up to the gel point. However, in all these studies, the data were acquired after the reaction had been slowed down dramatically by using very low thrombin concentrations, making a direct comparison with our results difficult.

In any case, to better assess the validity of different polymerization schemes, (macro)molecular models are necessary. Both Müller and Burchard and Wiltzius and coworkers used only simple rigid rod-like models, whereas we have considerably extended the modeling range by also including worm-like chains. In this respect, the first point that has to be clarified concerns the length of the fibrin monomer. From EM studies, the main FG body has a length of ~46–48 nm, as proposed long ago by Hall and Slayter (1959) and confirmed by several other studies (Mosesson et al., 1981; Erickson and Fowler, 1983; Weisel et al., 1985). These three latter studies have also provided evidence that the C-terminal portions of the Aα-chains likely fold back

from the outer domains to form a fourth domain positioned above the central one. Indeed, a 180° reversal of direction of the α-chain at the end of the coiled-coil has been found in the crystal structure of fragment D (Spraggon et al., 1997), providing further support for this hypothesis. However, in previous light scattering studies performed on FG (and fibrin oligomers) solutions, it was suggested that its length was between 75 and 100 nm (Müller et al., 1981; Wiltzius et al., 1982a; and references therein). Our MALLS data, collected on-line from an SE-HPLC separation of the starting FG solutions (Bernocco, 1998; Bernocco S., C. Cuniberti, and M. Rocco, in preparation), yielded an ~14.5–15 nm $(\langle R_g^2\rangle_z)^{1/2}$ value for fibrinogen from which a length of 50–52 nm could be derived, slightly higher but quite consistent with the EM data. Indeed, previous small-angle x-ray scattering work on bovine FG had yielded $(\langle R_g^2\rangle_z)^{1/2}$ values very close to ours (Lederer, 1972). The much higher values observed by Müller et al. (1981) could have resulted from high molecular-weight contaminants, because no size-exclusion chromatography step was apparently used in their sample preparation procedures. In addition, the presence of 0.1 M KCl instead of NaCl may have had unknown effects; indeed, their low M_L values for FG could be explained by a conformational transition to more elongated species involving the C-terminal portions of the α-chains (see below). As for Wiltzius et al. (1982a,b; and references therein), their 75-nm length for FG was mainly inferred from hydrodynamic data, whose interpretation highly depends on additional parameters such as the degree of hydration.

Therefore, our main models were built starting from a cylindrical monomer with a length of 50 nm and a diameter of ~3 nm, and were used to simulate RLSS and RLDS stiff polymers. The RLSS polymers were simulated because end-to-end interactions between sites apparently not directly affected by FPA removal may come into play. Evidence for the presence of such "D–D" long interaction sites has been offered (see Mosesson et al., 1995; and references therein), and, indeed, in the crystal structure of a proteolytic fragment derived from cross-linked fibrin termed double-D, such interactions are evident, albeit weak ones, considering the small amount of surface buried at the contact sites (Spraggon et al., 1997). Needless to say, the RLDS models conform to the accepted, classic fibrin polymerization model, but less rigid configurations were also explored by simulating WLDS chains, with persistence lengths varying from one to four monomer units (50–200 nm).

However, that a conformational transition to more elongated monomers may take place after FG activation cannot be excluded. Relatively recent literature data (Veklich et al., 1993; Gorkun et al., 1994), which confirmed and extended previous observations (Medved' et al., 1985), suggest that the C-terminal portions of the α-chains may break away from the central domain and interact intermolecularly. Thus, they may have a role in fibrin formation, although the removal of both FPA and FPB seems to be a prerequisite for this to happen. This was modeled using WLSS polymers in which the activated monomer length was expanded to 75 nm to match Wiltzius (1982a) data. For simplicity, a cylindrical shape was retained, with a reduced diameter to conserve the volume, and a l_p of one or two activated monomer units (75–150 nm) was used. Incidentally, the M_L for this model is close to that measured for FG by Müller and Burchard (1978).

Models for fibrin polymerization

As examined in detail in the Results section, the classic RLDS models do not fit the curves of $\langle R_g^2\rangle_z$ versus M_w presented in Fig. 9. In particular, the curves for the models obtained with the Flory theory are completely off target (Fig. 9, *A* and *D*), whereas those generated according to the theory of Janmey with $Q = 16$ seem to match only in the first ~50 s, after which they clearly diverge (Fig. 9, *B* and *E*). The RLSS models would perform slightly better only if the Flory theory would apply (Fig. 9, *A* and *D*), otherwise they would produce polymers with excessively high $\langle R_g^2\rangle_z$ values for a given M_w (data not shown). WLSS polymers, which could either form from D–D long interactions as for the RLSS case (WLSSQ16-50), or as a result of interactions between the αC domains (WLSS-75, WLSS-150, WLSSQ16-75), could be made to fit the entire data set by choosing appropriate persistence-length values. However, all these semiflexible single-stranded structures are at odds with the Casassa plots data, especially at times >70 s (see Fig. 8 *C*). Taken together, these data confirm previous light scattering observations on the inadequacy of the rigid double-stranded model for the early stages of the reaction, but also argue against rigid or semiflexible single-stranded polymers being the predominant species.

When WLDS polymers were then examined in the Janmey theory framework (Fig. 9, *B–C*, and relative insets), relatively good agreement could be found when a persistence length of 200 nm was used (WLDSQ16-200 curves). Moreover, with this l_p the Casassa plots will be more linear than the correspondent WLDS-50 polymers shown in Fig. 7, *E–H*, and closer to the RLDS ones, although the linearity should not extend below ~40°. Instead, the $\langle R_g^2\rangle_z$ versus M_w data computed from the distributions derived from EM data (Weisel et al., 1993) are only roughly consistent with the Flory RLDS simulations, which we have shown to be incompatible with most of our data. This behavior is not surprising, because non rate-limiting amounts of thrombin (100 NIH units/mg FG) were used by Weisel et al. (1993), and reinforces the notion of a strong enzymatic control of FG polymerization. As for the very high Q values, which were required to fit the EM data of Janmey et al. (1983b), the RLDSQ32 simulation included in Fig. 9 *B* seem to indicate otherwise. WLDS simulations with $Q = 32$ could be made to fit the data, but would require an unlikely quite short persistence length (data not shown). This would sug-

gest that the steps required to prepare a sample for EM may somewhat alter the polymer distribution, and cast doubts on the reliability of such kinetic data. In contrast, it is useful to compare, even roughly, our models with the EM evidence. For instance, with l_p = 200 nm, WLDS 20-mers and 40-mers would have $(\langle R_g^2 \rangle)^{1/2}$ values 20% and 30% shorter, respectively, than the corresponding stiff RLDS polymers. This translates into protofibrils with end-to-end distances shorter by the same amount in respect to rigid ones, somewhat at the limit but still compatible with the appearance of the twisted protofibrils seen by EM (Medved' et al., 1990; Weisel et al., 1993; and references therein), although no estimation of l_p was ever made from such samples that we are aware of. Lateral aggregation of the protofibrils would then reintroduce a higher degree of rigidity, but occasional bending points would remain, again in agreement with the EM data (for instance, see the recent images in Ryan et al., 1999).

Notwithstanding the good fit provided by the WLDSQ16-200 simulation, the M_L ratio computed for this polymer distribution is ~25% smaller than the one deduced from the Casassa plot after ~70 s (see Table 1), when we have shown that they should be reliable. Moreover, by this time M_L has already reached a plateau, a behavior not predicted by any simple bifunctional polymerization mechanism. The formation of FG–fibrin monomer complexes, confirmed by other light scattering studies (Brass et al., 1976; Brosstad et al., 1979), can at least partially account for this behavior (see Fig. 8 *C*). Indeed, an even better fitting with the $\langle R_g^2 \rangle_z$ versus M_w data was found when a rough simulation including this effect was carried out (WLDSQ16-200M, Fig. 9 *C*). However, the consequences of the formation of such intermediates on the protofibril structure and kinetics remain to be better ascertained.

It is also possible that we are not dealing with just one simple polymerization mechanism. For instance, a mixture of WLSS polymers, formed by the interactions between the αC domains, and of half-staggered WLDS polymers may be present simultaneously, with a distribution characterized by a lower Q value (incidentally, higher Q would decrease the M_L ratio for any given M_w value). It is conceivable that such a system could exhibit both linear Casassa plots, due to the presence of single-stranded species, and a higher M_L ratio, resulting from the lower Q value. A similar mechanism was hypothesized by Wiltzius et al. (1982b), but more data will be needed before fully exploring these more complicated simulations.

Finally, other possible, superimposed mechanisms would involve the lateral association between the preformed double-stranded fibrils, which is known to be enhanced by the release of FPB under near physiological conditions (see Di Stasio et al., 1998), and/or branching. Indeed, under our conditions, already 2% of the total of FPB is released after 60 s, increasing to 12% after 240 s (Profumo, A., S. Bernocco, G. Damonte, C. Cuniberti, and M. Rocco, in preparation). Thus, by the time the M_w has reached values around 1×10^6 g mol^{-1}, significant lateral aggregation, and possibly branching, could have started to take place. However, the data extracted from the Casassa plots seem to indicate otherwise, in agreement with previous observations showing the strong Ca^{2+}-dependence of the B–*b* interaction (Marx, 1988, and references therein), so at least this phenomenon should not be relevant under our experimental conditions. As for branching, it could be excluded if it happens only as a consequence of lateral aggregation; EM evidence to the contrary has been presented (Mosesson et al., 1993), but at higher ionic strengths (I = 0.3–0.4) than the one used in our study (I = 0.15).

CONCLUDING REMARKS

In conclusion, with our stopped-flow MALLS set-up, we have been able to measure some important structural parameters of fibrin polymers for the very early stages of the thrombin-catalyzed reaction. These studies were carried out in the absence of calcium and in the presence of EDTA-Na_2, and therefore their relevance to the real physiological process has to be better ascertained. Under our conditions, we have found that WLDS semiflexible fibrils with a persistence length of about 200 nm provide a good description of the experimental data. The most notable discrepancy is a 25% lower and slowly increasing M_L ratio compared to the almost flat curve shown by the experimental data at relatively short times (>70 s). The formation of FG-fibrin monomer complexes could partially account for this behavior. However, it cannot be excluded that the polymerization may proceed by at least two different, either sequential or overlapping, elongation mechanisms (single- and double-stranded), both dependent on the FPA cleavage, but the unraveling of these events will require additional experiments and modeling. Along this line, further studies are in progress to investigate a wider FG concentration range, the influence of the removal of the αC extensions, different thrombin/substrate ratios, and the effects of preferential release of just one pair of fibrinopeptides induced by snake venoms coagulating enzymes.

Note added in revision: After submitting the revised version of this manuscript, we became aware of the publication of the crystal structure of a fibrinogen large fragment, by Brown et al. (Brown, J. H., N. Volkmann, G. Jun, A. H. Henschen-Edman, and C. Cohen. 2000. The crystal structure of modified bovine fibrinogen. *Proc. Natl. Acad. Sci. USA.* 97:85–90). In this paper, evidence for flexibility along fibrinogen main body is given, lending further support for the worm-like protofibril model presented here.

This work was partially supported by grants from the Agenzia Spaziale Italiana to M.R., from the Consiglio Nazionale delle Ricerche to F.F., and from the Ministero Italiano della Ricerca Scientifica e Tecnologica to C.C.

We thank G. Levi, M. Bolognesi, R. Cancedda, and G. Arcòvito for support, W. Nieuwenhuizen for the generous gift of the Y18 monoclonal antibody, and G. Arcòvito, F. Andreasi-Bassi, M. De Spirito, and D. S. Cannell for stimulating discussions. We are deeply indebted to R. F.

Doolittle, L. Medved' and B. Zimm for kindly reading the original manuscript and providing comments and suggestions, and to M. Mosesson for also carefully reviewing it.

REFERENCES

Bale, M. D., P. A. Janmey, and J. D. Ferry. 1982. Kinetics of formation of fibrin oligomers. II. Size distributions of ligated oligomers. *Biopolymers.* 21:2265–2277.

Bauer, R., S. L. Hansen, G. Jones, E. Suenson, S. Thorsen, and L. Øgendal. 1994. Fibrin structures during tissue-type plasminogen activator-mediated fibrinolysis studied by laser light scattering: relation to fibrin enhancement of plasminogen activation. *Eur. Biophys. J.* 23:239–252.

Belitzer, W. A., and J. L. Chodorova. 1952. On the nature of the conversion of fibrinogen to fibrin. *Biochimija (USSR).* 17:676–683.

Benoit, H., and P. Doty. 1953. Light scattering from non-Gaussian chains. *J. Phys. Chem.* 57:958–963.

Bernocco, S. 1998. Struttura del fibrinogeno e dei suoi oligomeri in soluzione (Solution structure of fibrinogen and its oligomers). Ph.D. thesis. Università degli Studi di Genova, Genova, Italy.

Blombäck, B. 1996. Fibrinogen and fibrin—proteins with complex roles in hemostasis and thrombosis. *Thromb. Res.* 83:1–75.

Brass, E. P., W. B. Forman, R. V. Edwards, and O. Lindan. 1976. Fibrin formation: the role of the fibrinogen–fibrin monomer complex. *Thromb. Heamost.* 36:37–48.

Brosstad, F., P. Kierulf, and H. C. Godal. 1979. The fibrin-solubilizing effect of fibrinogen as studied by light scattering. *Thromb. Res.* 14: 705–712.

Carr, M. E., Jr., L. L. Shen, and J. Hermans. 1977. Mass-length ratio of fibrin fibers from gel permeation and light scattering. *Biopolymers.* 16:1–15.

Casassa, E. F. 1955. Light scattering from very long rod-like particles and an application to polymerized fibrinogen. *J. Chem. Phys.* 23:596–597.

Di Stasio, E., C. Nagaswami, J. W. Weisel, and E. Di Cera. 1998. Cl^- regulates the structure of the fibrin clot. *Biophys. J.* 75:1973–1979.

Doolittle, R. F. 1984. Fibrinogen and fibrin. *Annu. Rev. Biochem.* 53: 195–229.

Edwards, F. B., R. B. Rombauer, and B. J. Campbell. 1969. Thiol-disulfide interchange reactions between serum albumin and disulfides. *Biochim. Biophys. Acta.* 194:234–245.

Erickson, H. P., and W. E. Fowler. 1983. Electron microscopy of fibrinogen, its plasmic fragments and small polymers. *In* Molecular Biology of Fibrinogen and Fibrin. M. W. Mosesson and R. F. Doolittle, editors. Annals of the New York Academy of Sciences, Vol. 406. New York. 146–163.

Everse, S. J., G. Spraggon, L. Veerapandian, M. Riley, and R. F. Doolittle. 1998. Crystal structure of fragment double-D from human fibrin with two different bound ligands. *Biochemistry.* 37:8637–8642.

Ferry, J. D. 1952. The mechanism of polymerization of fibrinogen. *Proc. Natl. Acad. Sci. USA.* 38:566–569.

Flory, P. J. 1936. Molecular size distribution in linear condensation polymers. *J. Am. Chem. Soc.* 58:1877–1885.

Flory, P. J. 1940. Kinetics of the degradation of polyesters by alcohols. *J. Am. Chem. Soc.* 62:2255–2261.

Flory, P. J. 1942. Molecular size distribution in linear condensation polymers. *J. Am. Chem. Soc.* 64:3067 (correction).

Flory, P. J. 1953. Principles of Polymer Chemistry. Cornell University Press, Ithaca, NY.

Forziati, A. F. 1950. Refractive index as a function of wavelength for sixty API-NBS hydrocarbons. *J. Res. Natl. Bur. Stan.* 44:373–385.

Forziati, A. F., D. L. Camin, and F. D. Rossini. 1950. Density, refractive index, boiling point and vapor pressure of eight monoolefin (1-alkene), six pentadiene and two cyclomonoolefin hydrocarbons. *J. Res. Natl. Bur. Stan.* 45:406–410.

Fowler, W., R. R. Hantgan, J. Hermans, and H. P. Erickson. 1981. Structure of the fibrin protofibril. *Proc. Natl. Acad. Sci. USA.* 78:4872–4876.

Geiduschek, E. P., and A. M. Holtzer. 1958. Application of light scattering to biological systems. *Adv. Biol. Med. Phys.* 6:431–551.

Gorkun, O. V., Y. I. Veklich, L. V. Medved, A. H. Henschen, and J. W. Weisel. 1994. Role of the αC domains of fibrin in clot formation. *Biochemistry.* 33:6986–6997.

Hall, C. E., and H. S. Slayter. 1959. The fibrinogen molecule: its size, shape and mode of polymerization. *J. Biophys. Biochem. Cytol.* 5:11–17.

Hantgan, R. R., and J. Hermans. 1979. Assembly of fibrin. A light scattering study. *J. Biol. Chem.* 254:11272–11281.

Harding, S. E., D. B. Sattelle, and V. A. Bloomfield (editors). 1992. Biochemical Applications of Laser Light Scattering. Elsevier, Amsterdam.

Huglin, M. B. (editor). 1972. Light Scattering from Polymer Solutions. Academic Press, London, New York.

Janmey, P. A. 1982. Kinetics of formation of fibrin oligomers. I. Theory. *Biopolymers.* 21:2253–2264. (note that, in this paper, ref. 14 is incorrect).

Janmey, P. A., M. D. Bale, and J. D. Ferry. 1983a. Polymerization of fibrin: analysis of light-scattering data and relation to a peptide release. *Biopolymers.* 22:2017–2019.

Janmey, P. A., L. Erdile, M. D. Bale, and J. D. Ferry. 1983b. Kinetics of fibrin oligomer formation observed by electron microscopy. *Biochemistry.* 22:4336–4340.

Kehl, M., F. Lottspeich, and A. Henshen. 1981. Analysis of human fibrinopeptides by high-performance liquid chromatography. *Hoppe-Seyler's Z. Physiol. Chem.* 362:1661–1664.

Knoll, D., R. R. Hantgan, J. Williams, J. McDonagh, and J. Hermans. 1984. Characterization of soluble polymerized fibrin formed in the presence of excess fibrinogen fragment D. *Biochemistry.* 23:3708–3715.

Koppert, P. W., C. M. G. Huijsmans, and W. Nieuwenhuizen. 1985. A monoclonal antibody, specific for human fibrinogen, fibrinopeptide A-containing fragments and not reacting with free fibrinopeptide A. *Blood.* 66:503–507.

Koyama, R. 1973. Light scattering of stiff chain polymers. *J. Phys. Soc. Jpn.* 34:1029–1038.

Laemmli, U. K. 1970. Cleavage of structural proteins during the assembly of the head of bacteriophage T4. *Nature.* 227:680–685.

Lange, M. 1967. Handbook of Chemistry. McGraw-Hill, New York. p. 1382.

Laurent, T. C., and B. Blombäck. 1958. On the significance of the release of two different peptides from fibrinogen during clotting. *Acta Chem. Scand.* 12:1875–1877.

Lederer, K. 1972. Small angle X-ray scattering measurements with dilute solutions of bovine fibrinogen. *J. Mol. Biol.* 63:315–320.

Li, X., D. Galanakis, and D. A. Gabriel. 1996. Transient intermediates in the thrombin activation of fibrinogen. Evidence for only the desAA species. *J. Biol. Chem.* 271:11767–11771.

Martinelli, R. A., and H. A. Scheraga. 1980. Steady-state kinetic study of the bovine thrombin–fibrinogen interaction. *Biochemistry.* 19: 2343–2350.

Marx, G. 1988. Mechanism of fibrin coagulation based on selective, cation-driven, protofibril association. *Biopolymers.* 27:763–774.

Medved', L. V., O. V. Gorkun, and P. L. Privalov. 1983. Structural organization of the C-terminal parts of fibrinogen Aα-chains. *FEBS Lett.* 160:291–295.

Medved', L. V., O. V. Gorkun, V. F. Manyakov, and V. A. Belitser. 1985. The role of fibrinogen αC-domains in the fibrin assembly process. *FEBS Lett.* 181:109–112.

Medved', L. V., T. Ugarova, Y. Veklich, N. Lukinova, and J. W. Weisel. 1990. Electron microscope investigation of the early stages of fibrin assembly. Twisted protofibrils and fibers. *J. Mol. Biol.* 216:503–509.

Mihalyi, M. 1968. Physicochemical studies of bovine fibrinogen. IV. Ultraviolet absorption and its relation to the structure of the molecule. *Biochemistry.* 7:208–223.

Mosesson, M. W. 1990. Fibrin polymerization and its regulatory role in hemostasis. *J. Lab. Clin. Med.* 116:8–17.

Mosesson, M. W., J. P. DiOrio, K. R. Siebenlist, J. S. Wall, and J. F. Hainfeld. 1993. Evidence for a second type of fibril branch point in fibrin polymer networks, the trimolecular junction. *Blood.* 82: 1517–1521.

Mosesson, M. W., and R. F. Doolittle. (editors). 1983. Molecular Biology of Fibrinogen and Fibrin. Annals of the New York Academy of Sciences, Vol. 406. New York.

Mosesson, M. W., J. Hainfeld, J. Wall, and R. H. Haschemeyer. 1981. Identification and mass analysis of human fibrinogen molecules and their domains by scanning transmission electron microscopy. *J. Mol. Biol.* 153:695–718.

Mosesson, M. W., K. R. Siebenlist, J. P. DiOrio, M. Matsuda, J. F. Hainfeld, and J. S. Wall. 1995. The role of fibrinogen D domain intermolecular association sites in the polymerization of fibrin and fibrinogen Tokyo II (γ275 Arg→Cys). *J. Clin. Invest.* 96:1053–1058.

Müller, M., and W. Burchard. 1978. Fibrinogen–fibrin transformations characterized during the course of reaction by their intermediate structures. A light scattering study in dilute solution under physiological, conditions. *Biochim. Biophys. Acta.* 537:208–225.

Müller, M., H. Lasarcyk, and W. Burchard. 1981. Fibrinogen–fibrin transformation. 2. Influence of temperature, pH and of various enzymes on the intermediates. *Int. J. Biol. Macromol.* 3:19–24.

Nelb, G. W., G. W. Kamykowski, and J. D. Ferry. 1980. Kinetics of ligation of fibrin oligomers. *J. Biol. Chem.* 255:6398–6402.

Ryan, E. A., L. F. Mockros, J. W. Weisel, and L. Lorand. 1999. Structural origins of fibrin clot rheology. *Biophys. J.* 77:2813–2826.

Shainoff, J. R., and I. H. Page. 1962. Significance of cryoprofibrin in fibrinogen–fibrin conversion. *J. Exp. Med.* 116:687–707.

Sheraga, H. A., and M. Laskowski, Jr. 1957. The fibrinogen–fibrin conversion. *Adv. Prot. Chem.* 12:1–131.

Schmitz, K. S. 1990. An Introduction to Dynamic Light Scattering by Macromolecules. Academic Press, London.

Schulz, G. V., and H. A. Ende. 1963. Oher einige thermodynamische Eigen schaften von Fibrinogenlösungen und Gund der Lichtstreuungsmethode. *Z. Phys. Chem.* 36:82–96.

Spraggon, G., S. J. Everse, and R. F. Doolittle. 1997. Crystal structures of fragment D from human fibrinogen and its crosslinked counterpart from fibrin. *Nature.* 389:455–462.

Timmermans, J. 1965. Physico-chemical constants of pure organic compounds, Vol. II. Elsevier, Amsterdam. p. 100.

Towbin, H., T. Staehelin, and J. Gordon. 1979. Electrophoretic transfer of proteins from polyacrylamide gels to nitrocellulose sheets: procedure and some applications. *Proc. Natl. Acad. Sci. USA.* 76:4350–4354.

Veklich, Y. I., O. V. Gorkun, L. V. Medved, W. Nieuwenhuizen, and J. W. Weisel. 1993. Carboxyl-terminal portions of the α-chains of fibrinogen and fibrin. Localization by electron microscopy and the effects of isolated αC fragments on polymerization. *J. Biol. Chem.* 268: 13577–13585.

Visser, A., and T. A. Payens. 1982. On the kinetics of the thrombin-controlled polymerization of fibrin. *FEBS Lett.* 142:35–38.

Weisel, J. W. 1986. Fibrin assembly. Lateral aggregation and the role of the two pairs of fibrinopeptides. *Biophys. J.* 50:1079–1093.

Weisel, J. W., and C. Nagaswami. 1992. Computer modeling of fibrin polymerization kinetics correlated with electron microscope and turbidity observations: clot structure and assembly are kinetically controlled. *Biophys. J.* 63:111–128.

Weisel, J. W., C. V. Stauffacher, T. E. Bullit, and C. Cohen. 1985. A model for fibrinogen: domains and sequence. *Science.* 230:1388–1391.

Weisel, J. W., Y. Veklich, and O. Gorkun. 1993. The sequence of cleavage of fibrinopeptides from fibrinogen is important for protofibril formation and enhancement of lateral aggregation in fibrin clots. *J. Mol. Biol.* 232:285–297.

Wiltzius, P., G. Dietler, W. Känzig, V. Hofmann, A. Häberli, and P. W. Straub. 1982a. Fibrin aggregation before sol-gel transition. *Biophys. J.* 38:123–132.

Wiltzius, P., G. Dietler, W. Känzig, A. Häberli, and P. W. Straub. 1982b. Fibrin polymerization studied by elastic and dynamic light-scattering as a function of fibrinopeptide A release. *Biopolymers.* 21:2205–2223.

Wyatt Technology Corporation. 1997. ASTRA Manual 4.50. Wyatt Technology Corporation, Santa Barbara, CA.

Yamakawa, H., and M. Fujii. 1974. Light scattering from wormlike chains. Determination of the shift factor. *Macromolecules.* 7:649–654.

Zimm, B. H. 1948. The scattering of light and the radial distribution functions of high polymer solutions. *J. Chem. Phys.* 16:1093–1116.